J. Fluid Mech. (1999), *vol.* 399, *pp.* 85–115. Printed in the United Kingdom

Secondary instability of crossflow vortices and swept-wing boundary-layer transition

By MUJEEB R. MALIK, FEI LI, MEELAN M. CHOUDHARI AND CHAU-LYAN CHANG

High Technology Corporation, PO Box 7262, Hampton, VA 23666, USA

(Received 23 July 1998 and in revised form 9 April 1999)

Crossflow instability of a three-dimensional boundary layer is a common cause of transition in swept-wing flows. The boundary-layer flow modified by the presence of finite-amplitude crossflow modes is susceptible to high-frequency secondary instabilities, which are believed to harbinger the onset of transition. The role of secondary instability in transition prediction is theoretically examined for the recent swept-wing experimental data by Reibert *et al.* (1996). Exploiting the experimental observation that the underlying three-dimensional boundary layer is convectively unstable, nonlinear parabolized stability equations are used to compute a new basic state for the secondary instability analysis based on a two-dimensional eigenvalue approach. The predicted evolution of stationary crossflow vortices is in close agreement with the experimental data. The suppression of naturally dominant crossflow modes by artificial roughness distribution at a subcritical spacing is also confirmed. The analysis reveals a number of secondary instability modes belonging to two basic families which, in some sense, are akin to the 'horseshoe' and 'sinuous' modes of the Görtler vortex problem. The frequency range of the secondary instability is consistent with that measured in earlier experiments by Kohama *et al.* (1991), as is the overall growth of the secondary instability mode prior to the onset of transition (e.g. Kohama *et al.* 1996). Results indicate that the N-factor correlation based on secondary instability growth rates may yield a more robust criterion for transition onset prediction in comparison with an absolute amplitude criterion that is based on primary instability alone.

1. Introduction

First-principles-based boundary-layer transition prediction requires the identification and prescription of the free-stream and wall disturbance field, quantitative determination of boundary-layer receptivity to this external forcing, computation of linear/nonlinear amplification of disturbances internalized in the boundary layer and careful consideration of the associated mechanisms of breakdown to turbulence. Therefore, transition prediction for configurations of practical significance is a daunting task, forcing designers to use simplified methods. Currently used transition prediction tools are based on the so-called e^N criterion that correlates the onset of transition with the logarithmic amplification ratio N of the most amplified linear instability mode. However, it is obvious that the receptivity phase, which determines the initial amplitudes of the boundary-layer disturbances (Tollmien–Schlichting (TS), crossflow, Görtler, Mack modes, etc.), needs to be accounted for in order to obtain accurate predictions of the transition onset location. In principle, the e^N criterion can be combined with any available information on the receptivity process, so as to

devise a new criterion that is based on the maximum local amplitude of the primary modes. In fact, the recently emerged parabolized stability equations (PSE) methodology could be used to even incorporate the effect of nonlinearity on the primary disturbance amplitude. An amplitude-based criterion then can be used to correlate transition onset.

Unfortunately, in spite of the extra physics included in the absolute amplitude criterion, a criterion of this type is deemed unsatisfactory, at least for the swept-wing case. In the absence of attachment-line contamination (Gaster 1967; Poll 1979), crossflow instability (Gregory, Stuart & Walker 1955) which can manifest itself in the from of both stationary and travelling disturbances (Poll 1985) is the dominant instability of the three-dimensional boundary layer on a swept wing. Experimental evidence from low-speed flows suggests that, in low-disturbance environments, stationary crossflow modes (commonly known as crossflow vortices) constitute the dominant primary instability as a result of the unavoidable surface roughness which can directly excite these stationary modes (e.g. Radeztsky *et al.* 1993). The apparently surprising forecast *vis-à-vis* the absolute amplitude criterion is linked to the strongly stabilizing influence of nonlinearity on stationary crossflow modes. The crossflow disturbance amplitude changes rather slowly with distance across the region of nonlinear disturbance development. Consequently, sensitivity of the predicted transition location to any uncertainties in the input data and/or the calculation process is bound to be substantial. A more robust criterion for transition correlation is, therefore, required.

The experimental observations by Kohama, Saric & Hoos (1991) in the Arizona State University (ASU) unsteady wind tunnel, and by Kohama, Onodera & Egami (1996) in a different facility, clearly show that the onset of laminar–turbulent transition is preceded by the appearance of rapidly growing high-frequency disturbances that ride on the quasi-saturated stationary vortex field. Measurements show that in the short streamwise region just upstream of the transition location, where the high-frequency modes are observed, the logarithmic amplification factor for these modes can approach a value of almost 9, in sharp contrast to the quasi-saturated evolution of stationary crossflow modes and the relatively slow growth of low-frequency travelling crossflow modes. In fact, Kohama *et al.* (1996) argue that 'the secondary instability plays a more important role than the primary instability in driving the boundary layer directly to a fully turbulent state'. This raises the interesting possibility of being able to predict the transition location on the basis of secondary instability analysis for a modified basic state that consists of the underlying boundary-layer flow plus the large-amplitude, quasi-saturated stationary crossflow vortices.

In this paper, we explore the above possibility within the limited scope of a small set of experiments performed in the low-speed ASU wind tunnel. For the conditions of the ASU experiment, we first compute (following the approach adopted by Malik & Li 1992, and Malik, Li & Chang 1994) the nonlinear evolution of stationary crossflow disturbances and find good agreement with the experimental data. The boundary-layer flow distorted by the presence of crossflow vortices is analysed for secondary instability modes. In particular, our aim is to uncover the relation, if any, between the linear growth of secondary instability modes and the observed locations of transition onset. Towards this goal, an N-factor correlation based on secondary instability modes has been developed and the pros and cons of this methodology relative to other transition prediction criteria are evaluated in terms of the respective accuracy levels and computational resources required.

In addition to this somewhat practical but clearly important goal, the paper studies secondary instability of stationary crossflow vortices. This part of our study is similar

to the earlier work done, for example, by Yu & Liu (1991, 1994), Hall & Horseman (1991) and Li & Malik (1995), but for Görtler vortices. Görtler vortices are counter-rotating vortices present in two-dimensional boundary layers over concave surfaces, while crossflow vortices are co-rotating and relevant in three-dimensional boundary layers. The present work shows that both seem to be subject to very similar secondary instabilities.

It is to be noted that we assume that the three-dimensional boundary layer we consider here is convectively unstable. Although some recent work (Lingwood 1995) has indicated that three-dimensional boundary layers may become absolutely unstable under certain circumstances, absolute instability is not an issue for the conditions of the ASU experiment. In swept-wing flows, 'pinch' points only occur in one spatial dimension while absolute instability requires pinch points to occur simultaneously in (α, ω)- and (β, ω)-planes. Therefore, the phrase 'absolute instability' can apply to the swept-wing flows (at least the infinite swept) only in a limited sense, e.g. 'chordwise absolute instability'. The works of Lingwood (1997) and Lin, Li & Malik (1999) (see also Malik 1997) show that, in swept-wing boundary layers, pinch points occur in the chordwise direction near the leading edge but only at relatively large leading-edge Reynolds numbers ($\overline{R} > 540$). Therefore, the underlying boundary-layer flow in the ASU experiment must be convectively unstable although, of course, the possibility that the mean flow distorted by the primary modes might be absolutely unstable cannot be ruled out without further investigation. Present results suggested a possible degeneracy of the temporal secondary instability modes. Mode crossings of this type have been previously investigated in the context of a flat-plate boundary layer (Koch 1992) and would only lead to algebraic growth.

The layout of the rest of the paper is as follows: we give a brief introduction to the experimental data in § 2; the numerical approach is given in § 3; results of the analysis are presented in § 4; § 5 gives a discussion of the results and the paper is concluded in § 6.

2. The ASU experiment

The linear and nonlinear evolution of stationary crossflow vortices on a 45° swept NLF(2)-0415 airfoil has recently been studied by Professor Saric and his coworkers in the Arizona State University Unsteady Wind Tunnel (Reibert *et al.* 1996; Carrillo, Reibert & Saric 1996). At the −4° angle-of-attack configuration employed during these experiments, the boundary-layer flow on the upper surface of the airfoil is subcritical to Tollmien–Schlichting instability waves and, hence, the laminar–turbulent transition process is dominated by the crossflow instability. A full-span array of roughness elements near the attachment line was used to introduce a spanwise-periodic pattern of stationary crossflow modes into the boundary layer. The downstream evolution of these modes was followed with detailed hot-wire measurements and naphthalene flow visualization. The parametric study included a systematic variation in both roughness spacing and roughness height at a selected set of Reynolds numbers, $Re = U_\infty C/\nu$ (where U_∞ is the free-stream velocity, C the airfoil streamwise chord and ν the kinematic viscosity). Let λ_z be the roughness spacing, k the roughness height, and $(X^*/C)_{tr}$ the position along the wing chord where transition occurs. Table 1 summarizes the test conditions examined by Reibert (1996), and Carrillo *et al.* (1996), respectively.

The following significant observations can be made from the data in table 1:

(i) The surface roughness spacing tends to have a strong influence on the transition onset location. For a fixed set of flow conditions, the transition onset location can

	Case	$Re\,(\times 10^{-6})$	λ_z (mm)	k (μm)	$(X^*/C)_{tr}$
(*a*)	I-A	2.4	12	6	0.52
	I-B	2.4	12	18	0.51
	I-C	2.4	12	48	0.49
	I-D	3.2	12	6	0.32
	I-E	3.2	12	18	0.30
	I-F	3.2	12	48	0.28
	I-G	2.4	36	6	0.49
(*b*)	II-A	2.4	18	6	0.50
	II-B	2.4	18	18	0.50
	II-C	2.4	18	48	0.50
	II-D	2.4	NA	NA	0.65
	II-E	2.4	8	6	0.70
	II-F	2.4	8	48	0.59

TABLE 1. Key data points from (*a*) Reibert (1996) and (*b*) Carrillo *et al.* (1996).

vary from 50% chord to 70% chord, depending on the spectral composition of the surface roughness distribution.

(ii) At a fixed roughness spacing that corresponds to the spanwise wavelength of the linearly most unstable stationary mode which, from linear PSE computations, is shown to be approximately 12 mm, increasing the roughness height (and, hence, the initial crossflow disturbance amplitude) produces an insignificant change in the transition onset location. This finding is common to both Reynolds numbers investigated during these experiments, although the overall location of transition onset is considerably farther upstream at the higher Reynolds number.

(iii) The growth of the naturally dominant stationary mode can be suppressed via artificial excitation of another stationary mode with a suitably different wavelength (e.g. Case II-E). In particular, by choosing a shorter roughness spacing, it is possible to delay the onset of transition beyond that in the natural case.

The detailed hot-wire measurements that accompanied the transition onset data in table 1 demonstrated the strong influence of nonlinear disturbance interactions on the amplitude evolution of stationary crossflow vortices over a significant range of chordwise locations.

Cases I-A–I-E, and II-E from table 1 have been selected for the current analysis. The first five cases illustrate both the relative insensitivity of transition onset location to roughness height for a fixed Reynolds number and fixed roughness spacing, and the upstream movement in the transition location when the Reynolds number is increased. Case II-E shows that transition can be delayed by exciting short-wavelength crossflow modes that do not undergo adequate amplification to cause the onset of transition, but can still suppress the growth of the naturally occurring stationary crossflow modes.

3. Numerical approach

3.1. *Basic flow*

We use a body-fitted orthogonal coordinate system where x^*, y^* and z^* denote chordwise, wall-normal and spanwise directions, respectively. For infinite swept wings, the basic flow is independent of the spanwise coordinate z^*. Therefore, quasi-three-

dimensional boundary-layer equations can be used to obtain the mean flow. The first-order boundary-layer equations can be written as

$$U^*\frac{\partial U^*}{\partial x^*} + V^*\frac{\partial U^*}{\partial y^*} = -\frac{1}{\rho^*}\frac{\partial P^*}{\partial x^*} + \nu^*\frac{\partial^2 U^*}{\partial y^{*2}}, \tag{3.1a}$$

$$U^*\frac{\partial W^*}{\partial x^*} + V^*\frac{\partial W^*}{\partial y^*} = \nu^*\frac{\partial^2 W^*}{\partial y^{*2}}, \tag{3.1b}$$

$$\frac{\partial U^*}{\partial x^*} + \frac{\partial V^*}{\partial y^*} = 0, \tag{3.1c}$$

where U^*, V^* and W^* are the velocity components in the chordwise, wall-normal and spanwise directions, respectively, and P^* is pressure, ρ^* the density and ν^* the kinematic viscosity. A similarity-transformed form of these equations was solved by a finite-difference method (Wie 1992) for the prescribed pressure distribution and subject to boundary conditions

$$y^* = 0, \quad U^* = V^* = W^* = 0, \tag{3.2a}$$

$$y^* \to \infty, \quad U^* \to U_e^*, \quad W^* \to W_e^*. \tag{3.2b}$$

All lengths and the mean flow quantities are made non-dimensional by suitable scales. Hence, we write

$$x = x^*/l, \quad y = y^*/l, \quad z = z^*/l,$$

$$\overline{u} = U^*/U_0, \quad \overline{v} = V^*/U_0, \quad \overline{w} = W^*/U_0, \quad \overline{p} = P^*/\rho^* U_0^2,$$

where l and U_0 represent the reference length based on boundary-layer thickness at a fixed location and the chordwise boundary-layer edge velocity at the same location, respectively. We note that x^* in (3.1) above represents chordwise surface distance while X^* in table 1 is the Cartesian coordinate defined such that $X^*/C = 1$ at the trailing edge of the wing with chord length C. we also define a Reynolds number R as

$$R = \frac{U_0 l}{\nu^*}.$$

3.2. *Parabolized stability equations*

The above basic flow is perturbed by fluctuations in the flow, i.e. the total field can be decomposed into a mean value (boundary-layer solution) and a perturbation quantity

$$u = \overline{u} + \tilde{u}, \quad v = \overline{v} + \tilde{v}, \quad w = \overline{w} + \tilde{w}, \quad p = \overline{p} + \tilde{p},$$

where the tilde denotes a perturbation quantity. We define $\boldsymbol{\phi}$ as

$$\boldsymbol{\phi} = (\tilde{u}, \tilde{v}, \tilde{w}, \tilde{p}), \tag{3.3}$$

where $\tilde{p}$ is the pressure perturbation and $\tilde{u}$, $\tilde{v}$, $\tilde{w}$ represent x, y, z components of velocity perturbations, respectively. The nonlinear disturbance equations can then be derived from Navier–Stokes equations and written as

$$\boldsymbol{\Gamma}\frac{\partial \boldsymbol{\phi}}{\partial t} + \boldsymbol{A}\frac{\partial \boldsymbol{\phi}}{\partial x} + \boldsymbol{B}\frac{\partial \boldsymbol{\phi}}{\partial y} + \boldsymbol{C}\frac{\partial \boldsymbol{\phi}}{\partial z} + \boldsymbol{D}\boldsymbol{\phi} - \left[\boldsymbol{E}_x\frac{\partial^2 \boldsymbol{\phi}}{\partial x^2} + \boldsymbol{E}_y\frac{\partial^2 \boldsymbol{\phi}}{\partial y^2} + \boldsymbol{E}_z\frac{\partial^2 \boldsymbol{\phi}}{\partial z^2}\right] = \boldsymbol{F}, \tag{3.4}$$

where the left-hand side contains only linear operators operating on the disturbance vector ϕ and the right-hand-side forcing vector $\boldsymbol{F}$ is due to nonlinear interaction and

includes all nonlinear terms associated with the disturbances. The right-hand side is given as

$$\boldsymbol{F} = -\tilde{\boldsymbol{A}}\frac{\partial \boldsymbol{\phi}}{\partial x} - \tilde{\boldsymbol{B}}\frac{\partial \boldsymbol{\phi}}{\partial y} - \tilde{\boldsymbol{C}}\frac{\partial \boldsymbol{\phi}}{\partial z} + \tilde{\boldsymbol{H}}\boldsymbol{\phi}. \tag{3.5}$$

In the above, $\boldsymbol{\Gamma}$ is the diagonal matrix $[1, 1, 1, 0]$ while $\boldsymbol{A}$, $\boldsymbol{B}$, $\boldsymbol{C}$ are given as

$$\boldsymbol{A} = \begin{bmatrix} \overline{u} & 0 & 0 & 1 \\ 0 & \overline{u} & 0 & 0 \\ 0 & 0 & \overline{u} & 0 \\ 1 & 0 & 0 & 0 \end{bmatrix}, \quad \boldsymbol{B} = \begin{bmatrix} \overline{v} & 0 & 0 & 0 \\ 0 & \overline{v} & 0 & 1 \\ 0 & 0 & \overline{v} & 0 \\ 0 & 1 & 0 & 0 \end{bmatrix}, \quad \boldsymbol{C} = \begin{bmatrix} \overline{w} & 0 & 0 & 0 \\ 0 & \overline{w} & 0 & 0 \\ 0 & 0 & \overline{w} & 1 \\ 0 & 0 & 1 & 0 \end{bmatrix},$$

and $\tilde{\boldsymbol{A}}$, $\tilde{\boldsymbol{B}}$, $\tilde{\boldsymbol{C}}$ are similar to $\boldsymbol{A}$, $\boldsymbol{B}$, $\boldsymbol{C}$ except that the overbar is replaced with a tilde and all ones are dropped. The coefficient matrices, $\boldsymbol{D}$, $\boldsymbol{E}_x$, $\boldsymbol{E}_y$, $\boldsymbol{E}_z$ are given as

$$\boldsymbol{D} = \begin{bmatrix} \overline{u}_x & \overline{u}_y & 0 & 0 \\ \overline{v}_x - 2\kappa\overline{u} & \overline{v}_y & 0 & 0 \\ \overline{w}_x & \overline{w}_y & 0 & 0 \\ 0 & 0 & 0 & 0 \end{bmatrix}, \quad \boldsymbol{E}_x = \boldsymbol{E}_y = \boldsymbol{E}_z = \begin{bmatrix} 1/R & 0 & 0 & 0 \\ 0 & 1/R & 0 & 0 \\ 0 & 0 & 1/R & 0 \\ 0 & 0 & 0 & 0 \end{bmatrix}.$$

The only non-zero component of the $\tilde{\boldsymbol{H}}$ matrix, for the present application, is

$$\tilde{\boldsymbol{H}}_{21} = \kappa\tilde{u}$$

where κ denotes the wall curvature. Any other curvature terms are of smaller order and can be dropped.

We assume that the given disturbance is periodic in time and in the spanwise direction; thus, the disturbance function $\boldsymbol{\phi}$ can be expressed by the following truncated Fourier series:

$$\boldsymbol{\phi} = \sum_{m=-M}^{M} \sum_{n=-N}^{N} \boldsymbol{\chi}_{mn}(x, y)\, \mathrm{e}^{\mathrm{i}(n\beta z - m\omega t)} \tag{3.6}$$

where M and N represent one-half the number of modes used in the analysis. Let λ_z be the dimensional spanwise wavelength and f be the dimensional disturbance frequency. The non-dimensional spanwise wavenumber is then denoted by $\beta = 2\pi l/\lambda_z$ and $\omega = 2\pi l f/U_0$ is the non-dimensional disturbance frequency. In the parabolized stability equation (PSE) approach (Herbert 1991; Bertolotti, Herbert & Spalart 1992; Chang *et al.* 1991), the variation of disturbance field along the chordwise direction (x) is decomposed into a fast-varying wave part and an amplitude function part:

$$\boldsymbol{\chi}_{mn}(x, y) = \boldsymbol{\Psi}_{mn}(x, y)\mathscr{A}_{mn}(x), \tag{3.7a}$$

$$\mathscr{A}_{mn}(x) = \exp\left(\mathrm{i}\int_{x_0}^{x} \alpha_{mn}(\overline{x})\,\mathrm{d}(\overline{x})\right), \tag{3.7b}$$

where $\boldsymbol{\Psi}_{mn}$ is the amplitude function for the Fourier mode $(m\omega, n\beta)$ defined as $\boldsymbol{\Psi}_{mn} = (\hat{u}_{mn}, \hat{v}_{mn}, \hat{w}_{mn}, \hat{p}_{mn})$ and α_{mn} is the associated streamwise wavenumber. The governing parabolized stability equations for mode (m, n) can be written as

$$\overline{\boldsymbol{G}}_{mn}\boldsymbol{\Psi}_{mn} + \overline{\boldsymbol{A}}_{mn}\frac{\partial \boldsymbol{\Psi}_{mn}}{\partial x} + \overline{\boldsymbol{B}}_{mn}\frac{\partial \boldsymbol{\Psi}_{mn}}{\partial y} = \boldsymbol{E}_y\frac{\partial^2 \boldsymbol{\Psi}_{mn}}{\partial y^2} + \boldsymbol{F}_{mn}/\mathscr{A}_{mn} \tag{3.8}$$

where matrices $\overline{\boldsymbol{E}}_{mn}$, $\overline{\boldsymbol{A}}_{mn}$ and $\overline{\boldsymbol{B}}_{mn}$ are given by

$$\overline{\boldsymbol{G}}_{mn} = -\mathrm{i}m\omega\boldsymbol{\Gamma} + \mathrm{i}\alpha_{mn}\boldsymbol{A} + \mathrm{i}n\beta\boldsymbol{C} + \boldsymbol{D} - \boldsymbol{E}_x\left(\mathrm{i}\frac{\mathrm{d}\alpha_{mn}}{\mathrm{d}x} - \alpha_{mn}^2\right) + n^2\beta^2\boldsymbol{E}_z,$$

$$\overline{\boldsymbol{A}}_{mn} = \boldsymbol{A} - 2\mathrm{i}\alpha_{mn}\boldsymbol{E}_x,$$

$$\overline{\boldsymbol{B}}_{mn} = \boldsymbol{B}.$$

In the above, the small terms such as $\mathrm{d}\alpha_{mn}/\mathrm{d}x$ can be neglected with essentially no effect on the results. The nonlinear forcing function $\boldsymbol{F}_{mn}$ is the Fourier component of the total forcing, $\boldsymbol{F}$, and can be evaluated by the Fourier series expansion

$$\boldsymbol{F}(x,y,z,t) = \sum_{m=-M}^{M-1}\sum_{n=-N}^{N-1}\boldsymbol{F}_{mn}(x,y)\,\mathrm{e}^{\mathrm{i}(n\beta z - m\omega t)}. \tag{3.9}$$

The Fourier decomposition in (3.7) can be done by using the fast Fourier transform (FFT) of $\boldsymbol{F}$, which is evaluated numerically in the physical space.

The boundary conditions for the above equations are

$$\hat{u}_{mn} = \hat{v}_{mn} = \hat{w}_{mn} = 0, \quad y = 0,$$

$$\hat{u}_{mn} \to 0, \quad \hat{v}_{mn}(m \neq 0,\ n \neq 0) \to 0, \quad \hat{w}_{mn} \to 0, \quad y \to \infty.$$

No free-stream boundary condition is required for the mean flow correction term $\hat{v}_{00}$.

For small disturbances, nonlinear forcing F can be set to zero and the linear PSEs (after dropping the subscript 11) can be written as

$$\overline{\boldsymbol{G}}\boldsymbol{\psi} + \overline{\boldsymbol{A}}\frac{\partial\boldsymbol{\psi}}{\partial x} + \overline{\boldsymbol{B}}\frac{\partial\boldsymbol{\psi}}{\partial y} = \boldsymbol{E}_y\frac{\partial^2\boldsymbol{\psi}}{\partial y^2}. \tag{3.10}$$

The solution of these equations requires the prescription of streamwise wavenumber α (see (3.7*b*)), which is determined by the following iterative procedure:

$$\alpha_{new} = \alpha_{old} - \mathrm{i}\int \boldsymbol{q}^\dagger\frac{\partial\boldsymbol{q}}{\partial x}\,\mathrm{d}y \Big/ \int |\boldsymbol{q}|^2\,\mathrm{d}y, \tag{3.11}$$

where $\boldsymbol{q} = (\hat{u},\hat{v},\hat{w})$ and $\dagger$ represents complex conjugate. As noted in Li & Malik (1996, 1997), associated with marching solution of (3.8) is the requirement that the term $\partial\hat{p}/\partial x$ be set to zero in the equation. Alternatively, large marching step sizes are required for a stable marching solution. Numerical experiments show that dropping the $\partial\hat{p}/\partial x$ term does not introduce significant error in the solution.

N-factors for the e^N correlation can be computed using

$$N = \int_{x0}^{x}\sigma\,\mathrm{d}x, \tag{3.12}$$

where σ is the disturbance growth rate and x_0 is the location of the onset of instability. For primary instability, the growth rate is taken to be $\sigma(x) = -\mathrm{Im}(\alpha(x))$ where α is the converged value from (3.11). For N-factors based upon secondary instability, growth rates are computed using the eigenvalue computations discussed in the subsection below.

3.3. *Secondary instability analysis*

The secondary instability analysis is performed locally at a fixed chordwise location using the temporal stability concept. Spatial analysis would be computationally more

involved and appeared to be outside the scope of the computational resources available to us. We rotate the coordinate system from (x, y, z) to (x_1, x_2, x_3) where x_1 and x_3 are aligned with the crossflow vortex and wave vector directions, respectively, and $x_2 = y$. The velocity components (boundary-layer plus crossflow disturbance) in the rotated coordinate system are denoted by U_1, U_2, and U_3 along the x_1, x_2, and x_3 directions, respectively.

We assume that the basic flow varies slowly along the x_1-axis and invoke the quasi-parallel assumption. The curvature of the vortex is also neglected. We consider a harmonic secondary disturbance of the form

$$\tilde{\phi}(x_1, x_2, x_3, t) = \phi'(x_2, x_3)\, \mathrm{e}^{\mathrm{i}(\alpha_s x_1 - \omega_s t)} + \text{c.c.}, \tag{3.13}$$

where α_s and ω_s are the wavenumber along x_1 and frequency of the secondary disturbance respectively. In the temporal framework, α_s is real and ω_s is complex. If $\omega_{si} > 0$, the secondary disturbance is unstable. For stationary crossflow vortices, the basic flow does not vary with time; therefore, the eigenfunction ϕ' is a function of (x_2, x_3) only. For a travelling crossflow disturbance, we use a coordinate system which convects with the wave; therefore, the disturbance appears stationary.

Using (3.13), one can derive a set of quasi-parallel, viscous, linear stability equations (see Malik *et al.* 1994) which yield eigenfunction structure in both x_2- and x_3-directions. We use the following boundary conditions at the wall and in the free stream:

$$u_1 = u_2 = u_3 = 0, \quad x_2 = 0, \tag{3.14a}$$

$$u_1 \to 0, \quad u_2 \to 0, \quad u_3 \to 0 \quad \text{as} \quad x_2 \to \infty. \tag{3.14b}$$

The computational domain is taken to be one wavelength of the crossflow disturbance in the x_3-direction and periodic boundary conditions are used

$$\phi'(x_2, x_3) = \phi'(x_2, x_3 + \lambda_p), \tag{3.14c}$$

where λ_p is the wavelength of the primary disturbance in the rotated coordinates obtained from α (3.11) and β (3.6). The governing equations along with the boundary conditions (3.14) constitute an eigenvalue problem governed by partial differential equations in two dimensions. Therefore, we call this a two-dimensional eigenvalue problem as in Lin & Malik (1996). The eigenvalue problem $\omega_s = \omega_s(\alpha_s)$ is numerically solved by using the Krylov subspace method (Lin, Wang & Malik 1996) which yields a number of eigenvalues which are then purified/confirmed by using the inverse Rayleigh iteration procedure.

4. Results and analysis

As stated in § 3.1, boundary-layer profiles were computed by using a finite-difference method. These calculations were carried out with both the theoretically determined pressure distribution (computed with the MCARF code (Stevens, Goradia & Braden 1971) and provided to us by Dr Reibert of Arizona State University) and that measured in the experiment (figure 1).

Although the PSE and secondary instability computations are carried out by solving the non-dimensional form of equations, comparisons require that the computational results be converted to appropriate dimensional quantities. In what follows, we will use a superscript * to indicate that the particular quantity is dimensional. Here, the results are first presented for the N-factors based on primary instability, followed by the nonlinear evolution of stationary disturbances. The mean flow modulated by

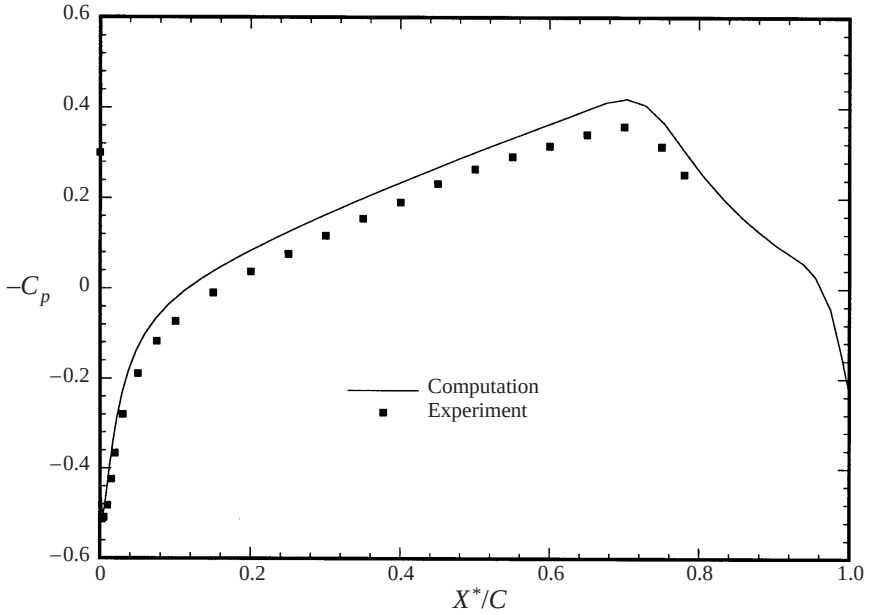

FIGURE 1. Comparison between computed and measured pressure coefficient, C_p, distributions.

		Travelling crossflow modes			Stationary crossflow modes	
$Re\,(\times 10^{-6})$	$(X^*/C)_{tr}$	N	Freq. (Hz)	λ_z (mm)	N	λ_z (mm)
2.4	0.5	11.0	100	13	7.74	12
3.2	0.3	10.5	200	8	7.3	9

TABLE 2. N-factor results for primary instability modes.

these stationary disturbances is then analysed for secondary instabilities. Transition correlations based on the nonlinearly computed primary disturbance amplitudes and secondary N-factors are then presented.

4.1. *N-factor correlation based on primary instability*

The N-factor curves based on linear growth rates of the (primary) stationary and travelling crossflow modes were computed using PSE (equations (3.10)–(3.12)). The N-factor correlations based on these results and the measured transition locations from table 1 are presented in table 2. The table also shows the spanwise wavelength which yields the highest N-factor at the transition location.

The N-factors based on the linear growth of primary disturbance modes are independent of the roughness height, being entirely determined by the Reynolds number involved. As such, this type of correlation cannot account for the significant measured shift in the transition location when the roughness parameters are varied. An absolute amplitude criterion that combines these N-factors with any available receptivity information (see Crouch 1997 for a related approach) has, in general, the potential to account for the influence of roughness size on transition location. However, a criterion of this type cannot explain the relative insensitivity of the

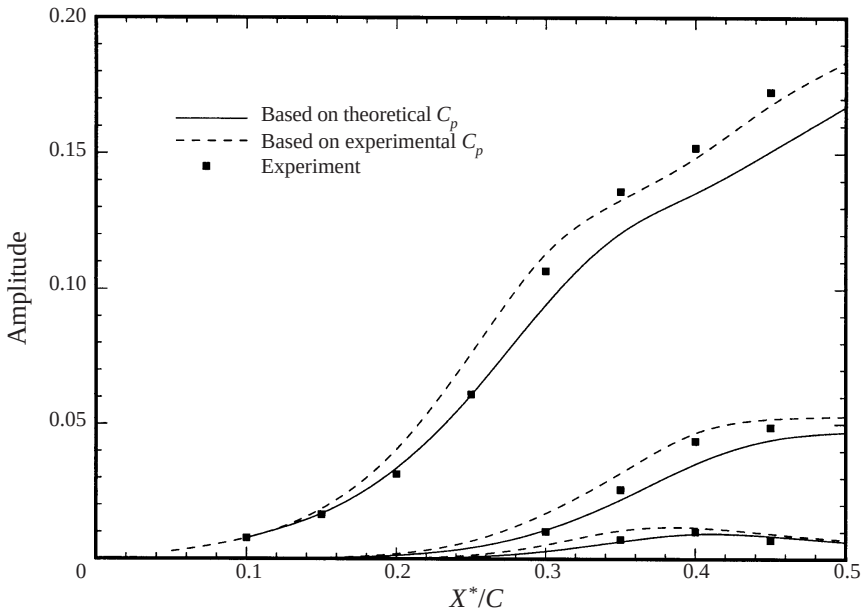

FIGURE 2. Comparison of measured and computed peak disturbance amplitudes (Case I-A).

transition location to the height of the artificial roughness observed in the ASU experiment referred to above. This insensitivity is attributed to the strongly nonlinear development of primary instability in the experiments by Reibert *et al.* (1996) and by Carrillo *et al.* (1996). Clearly, only those prediction methods which include some information about the initial disturbance spectrum and also retain the effects of disturbance nonlinearity can have the potential to explain the findings from the ASU experiment. Two of the main options that meet the above requirements are transition correlations based on the absolute amplitude of the primary disturbance and linear N-factors for the secondary instability of the boundary-layer flow distorted nonlinearly by the primary modes.

4.2. *Nonlinear evolution of stationary disturbances*

Nonlinear PSE calculations were carried out with boundary-layer profiles computed with both the theoretically determined pressure distribution and that measured in the experiment. In general, disturbance amplitude evolution computed using the measured distribution of the pressure coefficient, C_p, agreed better with the experimental data for large chordwise distances and large primary wave amplitudes where secondary instability is likely to set in. (See figure 2, wherein we have plotted the peak amplitudes of the fundamental and its two higher harmonics against the chordwise coordinate for Case I-A). Accordingly, all of the subsequent results in this paper are based on mean boundary-layer flow computed with the measured C_p distribution.

The PSE marching procedure was initiated slightly downstream of the attachment line location but upstream of the first hot-wire measurement station at $X^*/C = 0.05$. The effect of initial amplitude on the growth of the stationary disturbances with $\lambda_z = 12\,\text{mm}$ is shown in figure 3. When the initial amplitude for the chordwise velocity component is less than or equal to 10^{-6}, the nonlinear evolution differs little from the linear theory result within the computational domain. At such low initial amplitudes, the disturbances amplify by a factor of $e^{8.8}$ up to $X^*/C = 0.7$. When the

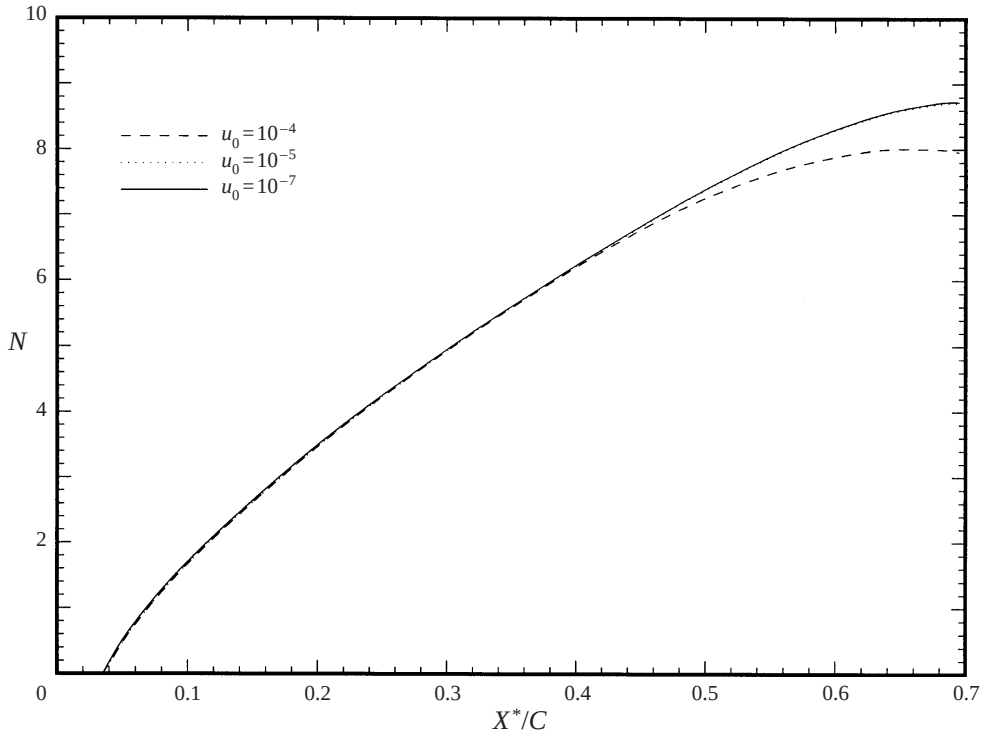

FIGURE 3. Effect of initial amplitude on the N-factor of stationary crossflow disturbances with $\lambda_z = 12\,\text{mm}$ for the ASU wing (using nonlinear PSE).

initial amplitude is 10^{-4}, the nonlinear PSE results begin to depart from the linear result at $X^*/C \approx 0.45$ where the disturbance has reached an amplitude of about 4%. The onset of nonlinear effects at crossflow amplitudes of around 4% is consistent with the results of Malik *et al.* (1994) for the swept Hiemenz flow.

Since the results for receptivity to the imposed roughness were not available, a suitable guess for the initial amplitude of the fundamental spanwise harmonic ($\lambda_z = 12\,\text{mm}$ for Cases I-A–I-E and $\lambda_z = 8\,\text{mm}$ for Case II-E) was used for the nonlinear PSE calculations described here. A total of 32 spanwise Fourier modes were included and the initial amplitudes of all higher harmonics (as well as of the mean flow correction) were set equal to zero for the calculations described in this paper. The adequacy of the number of Fourier modes was ascertained *a posteriori* by examining the decay of the computed disturbance spectrum at large wavenumbers. The guessed value of the initial fundamental amplitude was sequentially altered until the required match with the experimentally measured amplitudes was obtained. As described later, this usually involved a matching between the fundamental amplitudes at $X^*/C = 0.10$. A considerable effort was expended to convert the theoretically predicted disturbance velocity profiles to a form where a direct comparison could be made with the hot-wire data. In particular, a sequence of coordinate transformations was required to account for the two probe rotations (used to align the wire with the airfoil surface) and for the direction of hot-wire traversal. (See Reibert 1996 and Haynes 1996.) Hence, when we present the amplitudes of the primary waves, we mean the component of velocity in the direction in which the hot wire is most sensitive. This is usually different from $\tilde{u}$, $\tilde{v}$, or $\tilde{w}$.

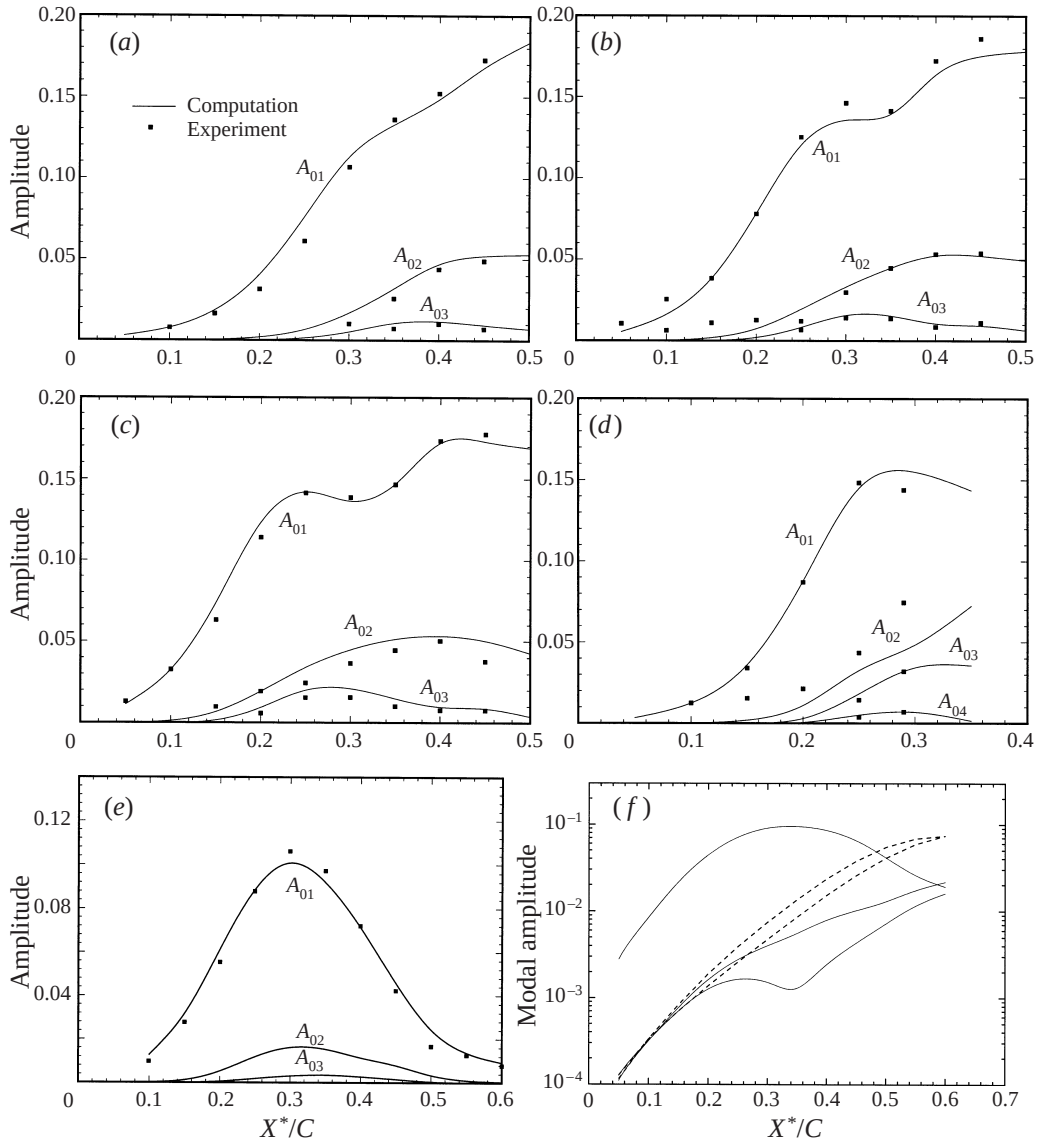

FIGURE 4. Comparison between computed and measured disturbance evolution. Peak modal amplitudes are plotted: (*a*) Case I-A; (*b*) Case I-B; (*c*) Case I-C; (*d*) Case I-D; (*e*) Case II-E; (*f*) Case II-E but the calculation is designed to show the suppression of naturally dominant crossflow modes in the presence of an artificially introduced 8.25 mm mode (top curve). For this case, the legend is as follows: solid lines: amplitudes of stationary modes with wavelengths of 16.5, 11, and 8.25 mm, respectively; dashed lines: amplitudes of 16.5 and 11 mm modes in the absence of the 8.25 mm mode.

Figure 4 shows the amplitudes of the fundamental and its two harmonics at the wall-normal location that corresponds to the peak in the disturbance profile for Cases I-A–I-D and II-E. The disturbance amplitudes have been scaled by the local boundary-layer edge velocity. In all cases except I-B and II-E, the initial disturbance amplitude was adjusted to match the experimental value of the fundamental amplitude at $X^*/C = 0.10$. An inspection of figure 4(*b*) indicates a local anomaly in the measured

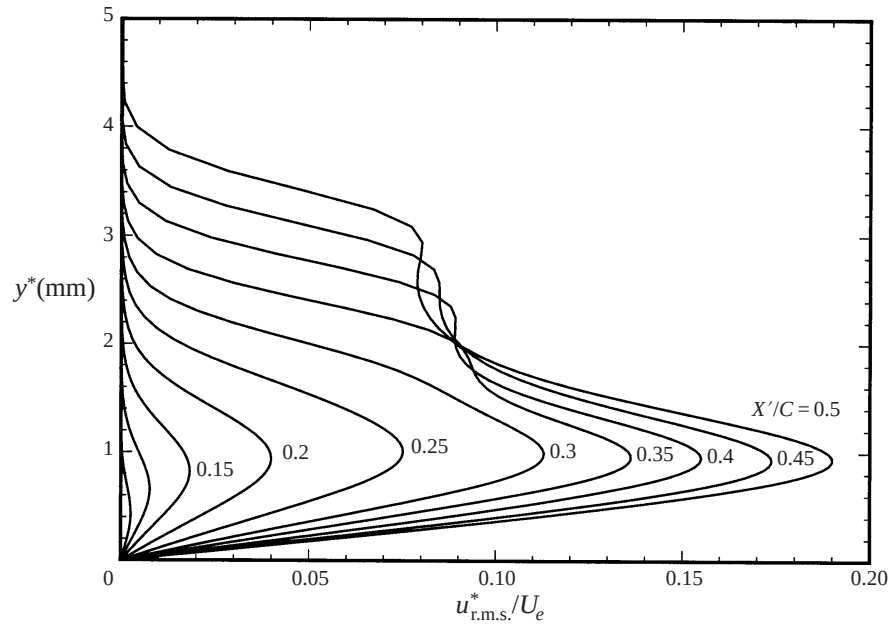

FIGURE 5. Disturbance mode shape profiles for Case I-A. Here, U_e is the local boundary-layer edge velocity.

fundamental at $X^*/C = 0.10$ for Case I-B; therefore, the amplitude at $X^*/C = 0.15$ was used to determine the appropriate initial amplitude for the PSE calculation. The remarkably good agreement between theory and the experimentally measured amplitudes is, in our opinion, a tribute to the care and thoroughness behind the ASU experiment. The computed disturbance mode-shape profiles (plotted in figure 5 for Case I-A) also exhibit the same features as the profiles measured during the experiment, as well as those computed by Malik *et al.* (1994) for the swept Hiemenz flow. Good agreement with the experimental data was also reported in the earlier calculations by Haynes & Reed (1996), although they used the computed C_p distribution (see figure 1) in their analysis. It may be noted here that, in spite of the strongly stabilizing influence of nonlinearity, the disturbance amplitude in Case I-A increases monotonically all the way up to the measured transition location. On the other hand, increased nonlinear effects in Cases I-B and I-C lead to a local plateau in amplitude evolution wherein the disturbance amplitude changes very slowly, and even (locally) decreases with X^*/C in Case I-C. The flat or non-monotonic character of amplitude evolution, found both in the experiment and computation, is an indication of the large uncertainty that would be inherent in a transition prediction method based on the absolute disturbance amplitude. The non-monotic character of amplitude evolution can also be found in the results presented by Malik *et al.* (1994) for the swept Hiemenz flow.

The computed disturbance evolution for Case I-D is shown in figure 4(*d*). In this case, experimental results are given at five chordwise locations as compared to eight to ten in Cases I-A–I-C. However, in the light of the good agreement for Cases I-A–I-C, it is not unreasonable to expect good agreement for Case I-D had more experimental points been given.

We next present nonlinear PSE results for Case II-E in figure 4(*e*). The fundamental mode in this calculation has a wavelength of 8 mm, i.e. the wavelength of the

forced roughness. The higher harmonics have wavelengths of 4, 8/3, 2, 8/5 mm, etc. Note that these do not contain the natural mode (with no intentional forcing) of 11 mm wavelength observed in the experiment. With these conditions specified, a faithful computer has no way of generating any perturbation with a component in the 11 mm mode. In order to obtain a better agreement with the measured peak amplitudes, the matching of the respective amplitudes in figure 4(*e*) was carried out at $X^*/C = 0.25$. Overall satisfactory agreement with the experimental data is observed in this case. However, some differences in r.m.s. amplitude (not shown) was noted in the downstream part of the measurement domain ($X^*/C > 0.40$). The measured amplitudes in the downstream region are dominated by naturally occurring crossflow modes with longer spanwise wavelengths which were not included in the calculation. However, the objective of the present analysis was to provide a theoretical explanation, based on secondary instability analysis, for the downstream shift in the transition onset location due to artificially introduced stationary crossflow disturbances. Accordingly, the secondary instability analysis for this case will be focused on the region upstream of 40% chord, wherein the stationary disturbance amplitudes are dominated by the artificially introduced disturbance.

In the experiment, the 8 mm mode is triggered by the roughness and has the largest amplitude initially, but the 11 mm mode will creep in because of some random excitation due to, perhaps, finer roughness on the wing surface introduced during the manufacturing process. We call a disturbance introduced this way the naturally occurring mode. Even though this mode has very small initial amplitude, it could eventually become the most significant mode because it has the largest growth rate. At this point, the computation starts to deviate (not shown) from the overall experimental results since the former do not contain all the modes.

In order to show that forcing a mode with 8 mm wavelength indeed suppresses the growth of the naturally occurring 11 mm mode (with wavelength close to the most amplified mode), we concocted a computational case with modal wavelengths of 33, 16.5, 11, 8.25 mm, etc. The 11 mm mode is chosen since a peak in the experimental spectrum is observed at this wavelength, downstream of $X^*/C \approx 0.4$. The 8.25 mm mode is close to the forced 8 mm mode. The results of this calculation are shown in figure 4(*f*) where the initial amplitude assigned to the 11 and 16.5 mm modes is an order of magnitude smaller than the 8.25 mm mode. It can be seen that the growth of the 11 and 16.5 mm modes slows down due to the presence of the 8.25 mm mode.

The disturbance evolution results for Case I-E have not been shown because detailed measurements of disturbance amplitudes were not available. The initial crossflow amplitude in this case was determined from the corresponding value for Case I-D, by assuming the receptivity to be a linear function of the roughness height. The accuracy of this assumption is largely inconsequential in this case, since the observed transition location is nearly insensitive to the initial disturbance amplitude.

Receptivity calculations would have eliminated the need for the rather *ad hoc* matching between the experimental and computed results presented above. However, the extra effort involved was deemed unnecessary since we are interested in the secondary instability of the mean flow modified by the presence of primary crossflow disturbances and the above mentioned matching procedure yields the 'correct' basic state for the secondary instability analysis. We note here in passing that the initial disturbance amplitudes needed to obtain good overall agreement with the experiments increased at a slower than linear rate when the roughness height was increased from 6 to 48 μm. This finding tends to indicate a nonlinear receptivity mechanism for the larger roughness heights used in the experiment.

4.3. *Secondary instability modes*

In general, nonlinear effects tend to reduce the amplification rate of a given crossflow vortex mode below its linear value, causing the vortex evolution to quasi-saturate at sufficiently large amplitudes. Because of the chordwise variation in the underlying boundary-layer flow, the saturation behaviour actually amounts to a relatively slow variation in the disturbance amplitude along the chordwise direction. The nonlinearly distorted mean flow, which exhibits a highly inflectional behaviour in the wall-normal and spanwise directions, typically supports high-frequency (i.e. an order of magnitude higher than the frequency range of travelling crossflow modes) secondary instability modes. As noted in § 3.3, the analysis of secondary instability modes is simplified by rotating the coordinate axes along the surface such that one of them (namely x_1) is aligned with the (approximate) direction of the vortex axis. After invoking the quasi-parallel assumption along this direction, one obtains a two-dimensional eigenvalue problem in the plane transverse to the vortex axis (i.e. the (x_2, x_3)-plane, where x_2 denotes the surface-normal coordinate and the x_3-axis is chosen to be normal to the vortex axis. Spatial discretization of the relevant partial differential equations leads to an algebraic eigenvalue problem that was solved for the complex frequency parameter ω_s as a function of real wavenumber α_s along the x_1-direction.

Results of the secondary instability analysis for Case I-A (i.e. $Re = 2.4 \times 10^6$, $\lambda_z = 12\,\text{mm}$, $k = 6\,\mu\text{m}$) are shown in figures 6(*a*)–6(*d*). Results were obtained at several locations but only those which correspond to chordwise locations of $X^*/C = 0.35$ and 0.45 are shown here. The (dimensional) temporal growth rates ($\text{Im}\,(\omega_s)U_0/l$) of the secondary instability modes are shown in figures 6(*a*) and 6(*c*); the corresponding phase velocity ($C_{ph} = \text{Re}\,(\omega_s)U_0/\alpha_s$) variation is indicated in figures 6(*b*) and 6(*d*). Similar results for Cases I-B–I-E, and II-E were obtained but are only shown for Case I-C here (figure 6*e*, *f*).

At locations where the stationary crossflow amplitudes are quite substantial, there exist as many as six or seven modes of secondary instability. An energy budget calculation (see below) indicates that the disturbance energy production of any given mode is typically dominated by energy transfer associated with either the surface-normal or the spanwise gradients of mean axial velocity distribution $U_1(x_2, x_3)$. Accordingly, each mode can usually be classified as being an 'x_2' or a 'x_3' mode. In practice, 'y' and 'z' are usually used to denote these directions, therefore we will also refer to these modes as 'y' and 'z' modes. This is akin to the 'horseshoe' and the 'sinuous' modes of the Görtler vortex problem (e.g. Swearingen & Blackwelder 1987; Li & Malik 1995).

Let us first analyse the secondary instability results for Cases I-A–I-C. The two dominant modes of secondary instability in each of these cases are found to be a 'y' mode and a 'z' mode, respectively. Typical eigenfunctions for these two classes of modes are illustrated in figures 7(*a*) and 7(*b*) respectively. For reference, contours of the mean axial velocity distribution $U_1(x_2, x_3)$ for the corresponding basic state are plotted in figure 8(*a*); the distributions of the shear rate in the x_2- and x_3-directions are shown in figures 8(*b*) and 8(*c*), respectively. The peak growth rates of the 'y' mode were generally found to be higher except in some regions where the 'z' mode had higher growth rate. The peak growth rates of the 'z' mode occur around a frequency of 3500 Hz, whereas the peak growth rates of the dominant 'y' mode occur near a somewhat higher frequency of 4500 Hz. The secondary instability frequency can, in general, be estimated by U_e/λ_p (assuming the phase speed $C_r = C_{ph}/U_e = 1$ and $\lambda_s = \lambda_p$) where λ_p is the wavelength of the primary disturbance. This rule of thumb yields a frequency of about 3 kHz, which is quite close to the computed values. The

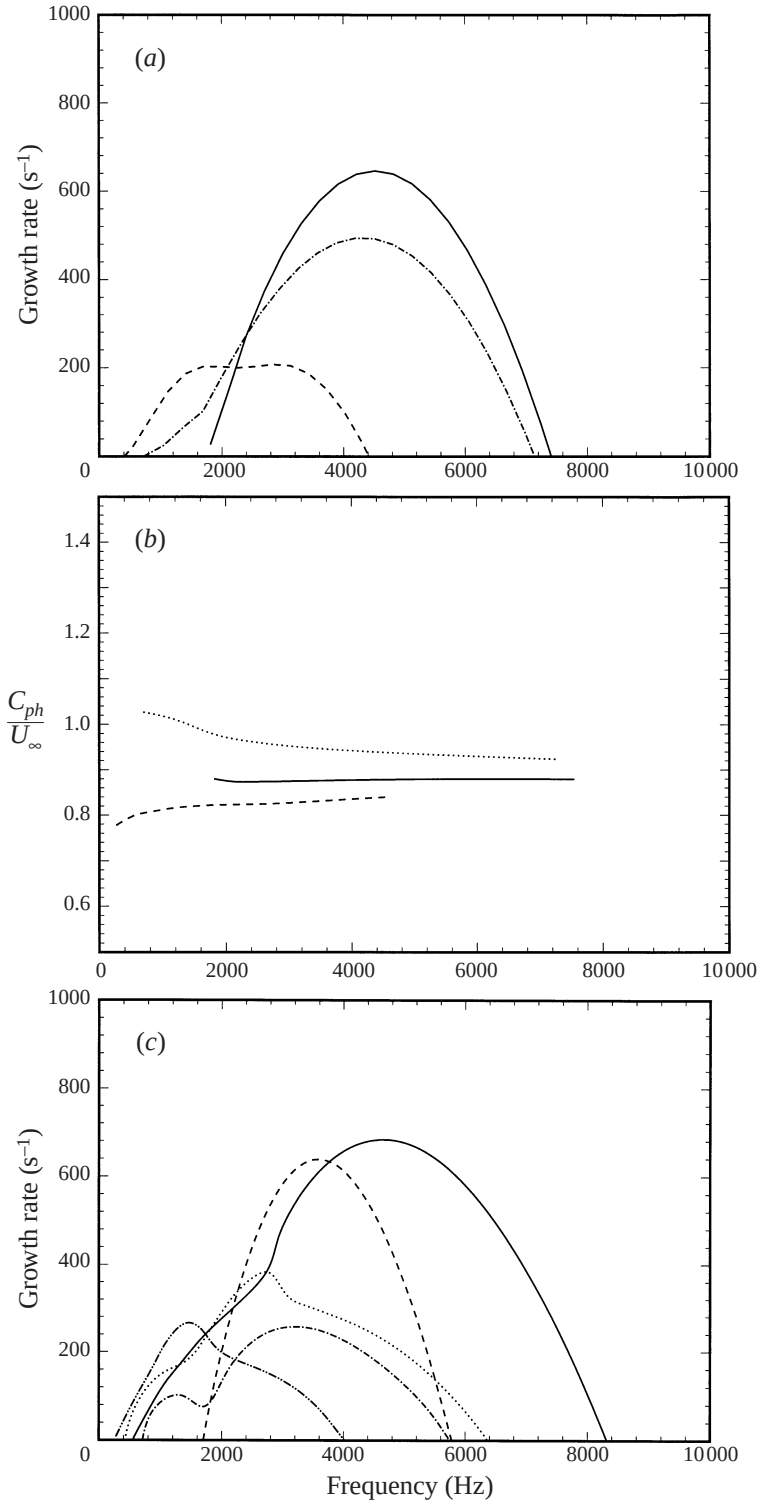

FIGURE 6 (*a–c*). For caption see page 102.

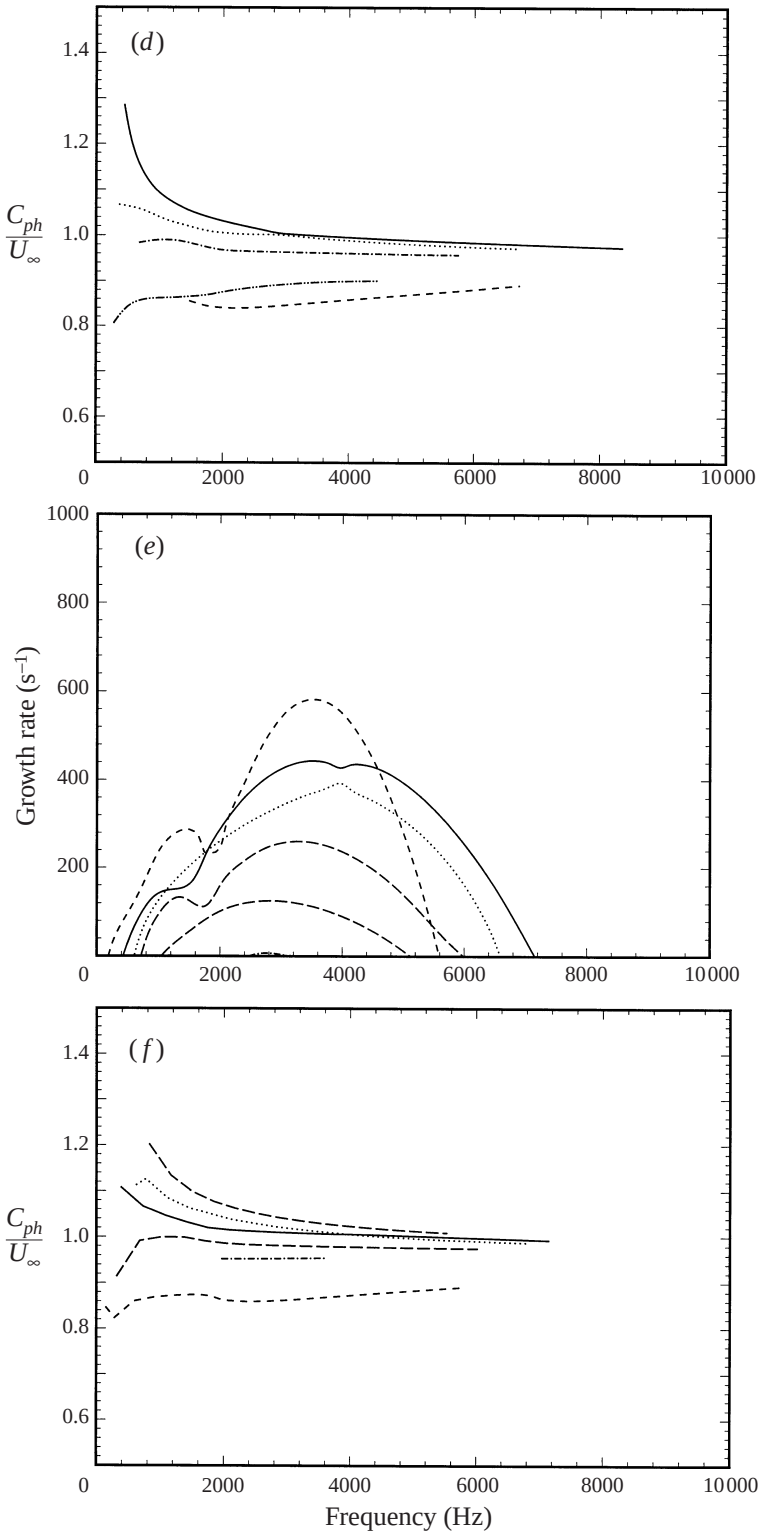

FIGURE 6 (*d–f*). For caption see page 102.

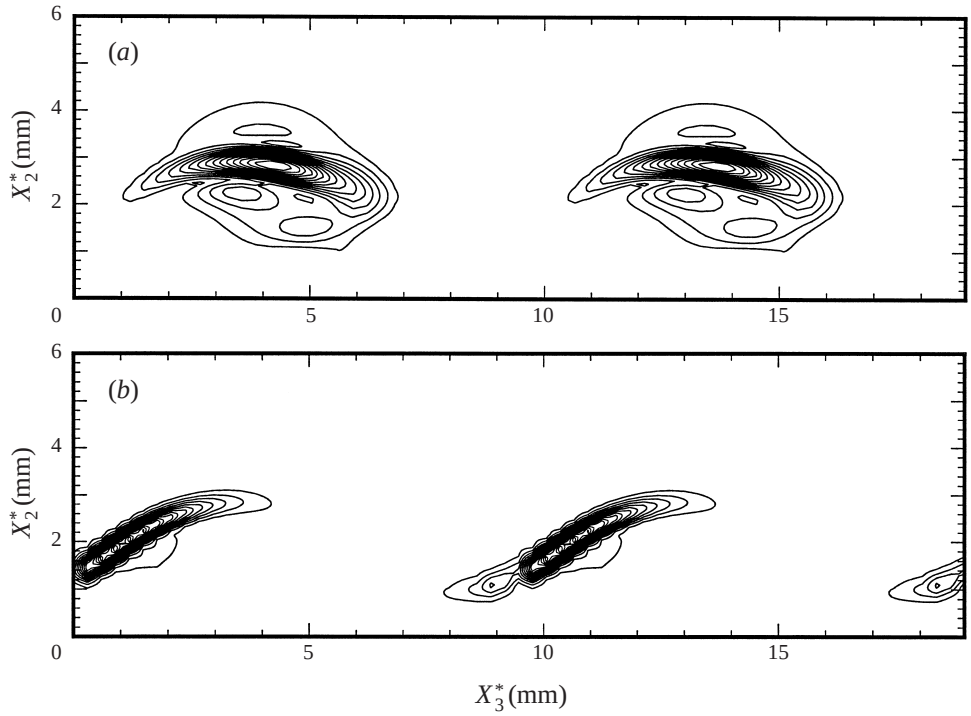

FIGURE 7. Magnitude of normalized axial velocity eigenfunction u_1 for the secondary instability mode at $X^*/C = 0.4$ for Case I-A (10 equispaced contours in the range $|u_1| \in [0.1, 1.0]$). (*a*) '*y*' mode; (*b*) '*z*' mode.

frequency range of the '*z*' modes is consistent with that measured by Kohama *et al.* (1991) in the same facility at slightly different values of Reynolds number and wavelength of dominant crossflow mode. Thus, it is likely that, in spite of the higher overall growth of the '*y*' mode, transition was actually caused by the '*z*' mode, possibly as a result of the peculiarities of the disturbance environment in the facility and/or the receptivity characteristics of the boundary-layer flow. Recent experimental results reported by Kawakami, Kohama & Okutsu (1999) show the secondary structure similar to that in figure 7(*b*), indicating that the '*z*' mode was observed in that experiment. For the relative importance of '*y*' and '*z*' modes in the Görtler vortex problem, the reader is referred to Li & Malik (1995). It appears that the state of the boundary layer, as modified by the crossflow vortices, may yield both '*y*'- and '*z*'-type modes. However, the parameters which give dominance to one or the other need further investigation. Since the experiment appears to favour the '*z*' mode, we will use this mode for the transition correlation studies whenever this mode is found to be substantially unstable in our computations.

In order to further understand the mechanism of secondary instability modes, we

FIGURE 6. Temporal growth rate (dimensional) and phase speed, C_{ph}/U_∞, of secondary instability modes. Here U_∞ is the free-stream velocity. The solid line represents the '*y*' mode. The other dominant mode (dashed line) is of '*z*' type. The dotted and dash-dot lines are for the additional secondary instability modes. (*a*, *b*) Case I-A, $X^*/C = 0.35$; (*c*, *d*) Case I-A, $X^*/C = 0.45$; (*e*, *f*) Case I-C, $X^*/C = 0.45$.

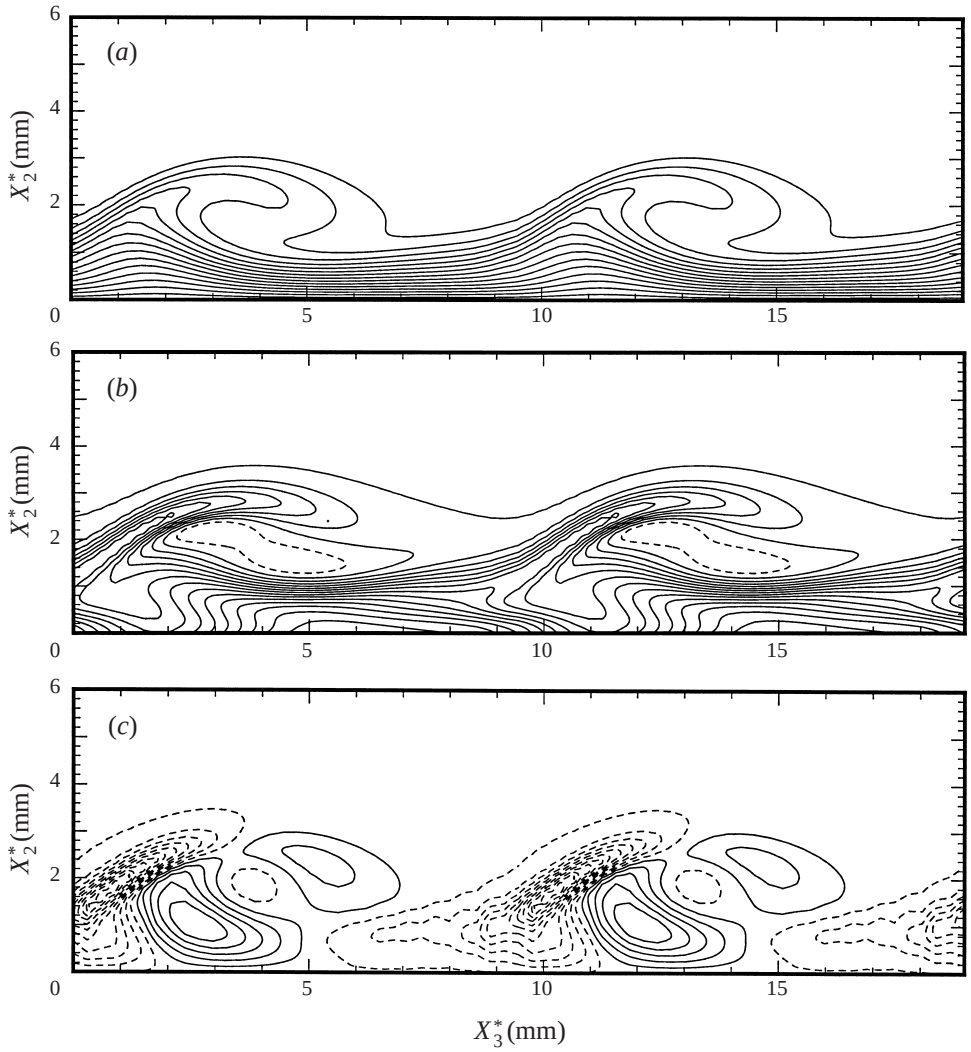

FIGURE 8. Contours of mean axial velocity distribution U_1, traverse shear and spanwise shear at $X^*/C = 0.4$ for Case I-A: (*a*) U_1 (22 equispaced contours in the range $U_1/U_\infty \in [005, 1.1]$; (*b*) $\partial U_1/\partial X_2$ (21 equispaced contours in the range $\partial U_1/\partial X_2 \in [-0.06, 1.34]$); (*c*) $\partial U_1/\partial X_3$ (16 equispaced contours at in the range $\partial U_1/\partial X_3 \in [-0.4, 0.2]$). Dashed contours show negative values.

consider the disturbance energy equation

$$\frac{\partial}{\partial t}\left(\frac{u_i u_i}{2}\right) + U_j \frac{\partial}{\partial x_j}\left(\frac{u_i u_i}{2}\right) = \frac{\partial}{\partial x_j}(-p u_i) + \frac{1}{R}\frac{\partial^2}{\partial x_j \partial x_j}\left(\frac{u_i u_i}{2}\right) - \frac{1}{R}\left(\frac{\partial u_i}{\partial x_i}\right)\left(\frac{\partial u_i}{\partial x_i}\right) - \frac{\partial U_i}{\partial x_j} u_i u_j, \qquad (4.1)$$

where $i = 1, 2, 3$. Integrating the above equation over one wavelength and across the boundary layer, we get

$$2\omega_{si} E = \frac{\mathrm{d}E}{\mathrm{d}t} = P - D, \qquad (4.2)$$

where $\omega_{si} = \mathrm{Im}(\omega_s)$ and the energy E is given by

$$E = \int_0^{2\pi/\beta_s} \int_0^{\infty} \int_0^{2\pi/\alpha_s} \left(\frac{u_i u_i}{2}\right) \mathrm{d}x_1\, \mathrm{d}x_2\, \mathrm{d}x_3, \tag{4.3}$$

production P by

$$P = -\int_0^{2\pi/\beta_s} \int_0^{\infty} \int_0^{2\pi/\alpha_s} u_i u_j \frac{\partial u_i}{\partial x_j}\, \mathrm{d}x_1\, \mathrm{d}x_2\, \mathrm{d}x_3. \tag{4.4}$$

and dissipation D by

$$D = \int_0^{2\pi/\beta_s} \int_0^{\infty} \int_0^{2\pi/\alpha_s} \frac{1}{R} \left(\frac{\partial u_i}{\partial x_j}\right) \left(\frac{\partial u_i}{\partial x_j}\right) \mathrm{d}x_1\, \mathrm{d}x_2\, \mathrm{d}x_3. \tag{4.5}$$

First we show in figure 9(a) that the growth rates obtained by the eigenvalue analysis and that from (4.2) above are quite close. Here, we only show the dominant y and z modes but similar results may be found for other modes. Figures 9(b) and 9(c) show the contribution of various production terms to y and z modes. It is clear that the dominant production term for the y mode is $-\langle u_1 u_2\rangle \partial U_1/\partial x_2$ while the dominant production term for the z mode is $-\langle u_1 u_3\rangle \partial U_1/\partial x_3$, where $\langle \bullet \rangle = \int_0^{2\pi/\alpha_s} \bullet\, \mathrm{d}x_1$. The contours of these dominant terms are plotted in figures 10(a) and 10(b), respectively. Comparison with figures 7(a) and 7(b) clearly shows the significance of the wall-normal shear for the y mode and the spanwise shear for the z mode.

The results presented earlier in figure 6(a–f) show that the overall growth characteristics of the secondary instability modes are rather intricate. Multiple peaks in the growth rate curve for a given mode of secondary instability are quite common. In some exceptional cases, one even finds a near coalescence between the local dispersion relationships for two different modes. Although this has not been further investigated here, a modal degeneracy of this kind would imply a combined algebraic and exponential growth for the instability model in the vicinity of the crossover location. The modal degeneracy of the secondary instability modes has also been noted by Koch (1992) in the context of Blasius flow and recently by Janke & Balakumar (1998) for a three-dimensional boundary layer.

The secondary instability results for Cases I-D and I-E (not shown) involve the higher chord Reynolds number of 3.2×10^6. Because of the relatively thinner boundary layers in these cases (due to both the higher Reynolds number and the upstream transition location), the gradients in the surface-normal direction are more important than the gradients along the vortex wavenumber (i.e. x_3) direction. This is probably why the secondary instability in Cases I-D and I-E primarily involved the 'y' type modes. Similarly, because of the increased free-stream speed and the thinner boundary layer, the band of most unstable secondary instability modes was observed to shift towards higher frequencies in the above two cases. We also note here that our earlier work (Malik, Li & Chang 1996) for Poll's (1985) swept-cylinder experiment found secondary disturbances in the neighbourhood of 17 kHz which is in good agreement with Poll's observations. These disturbances were found to be of 'y'-type in our computation. However, the experiment only recorded a high-frequency signal in the hot-wire trace without any explanation.

4.4. *Transition correlations based on the amplitude method and secondary N-factors*

The eigenvalue calculations described in § 4.3 were used to compute the N-factor curves (i.e. curves that depict the chordwise variation of spatial amplification ratio)

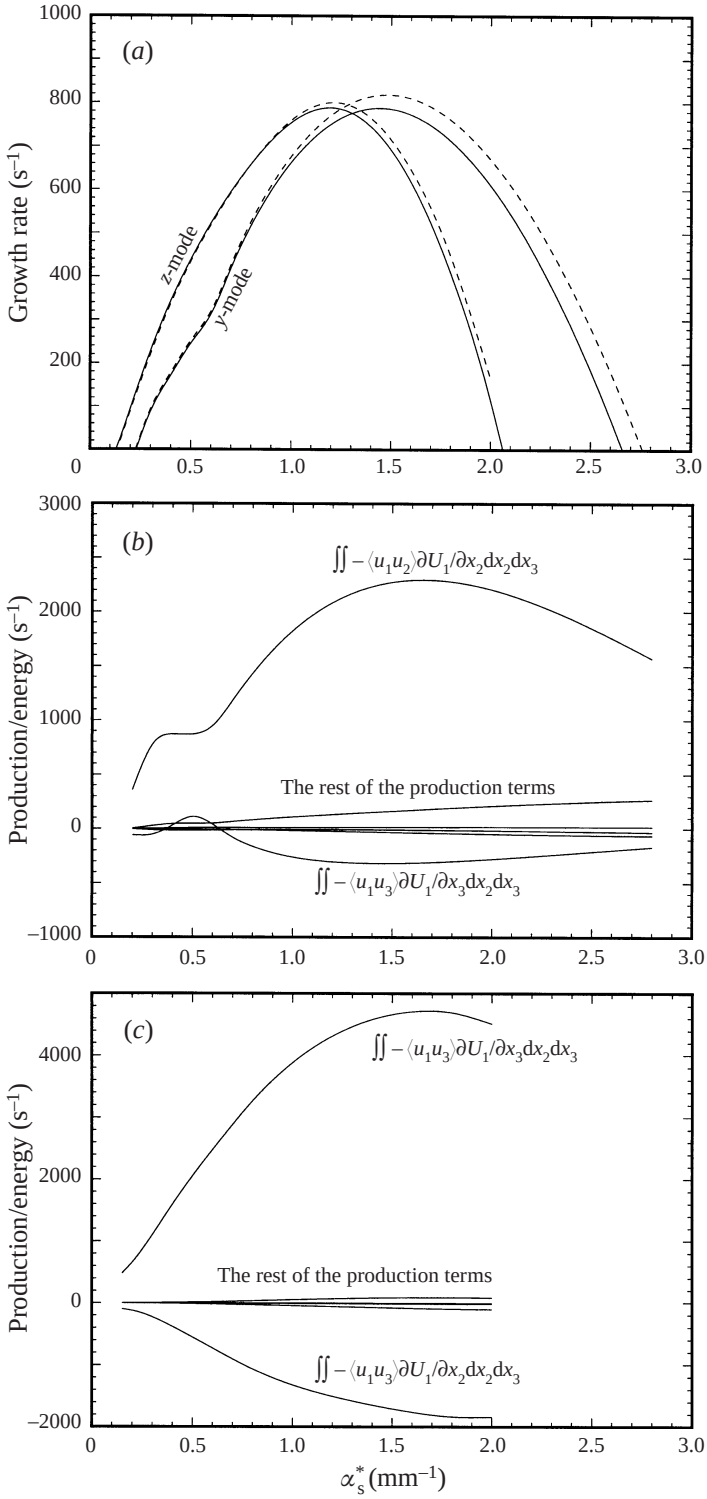

FIGURE 9. Secondary disturbance growth rate and various production terms for Case I-A at $X^*/C = 0.4$. (*a*) Growth rate from eigenvalue calculation (solid line) and the integral energy equation (dashed line); (*b*) production terms for the *y* mode; (*c*) production terms for the *z* mode.

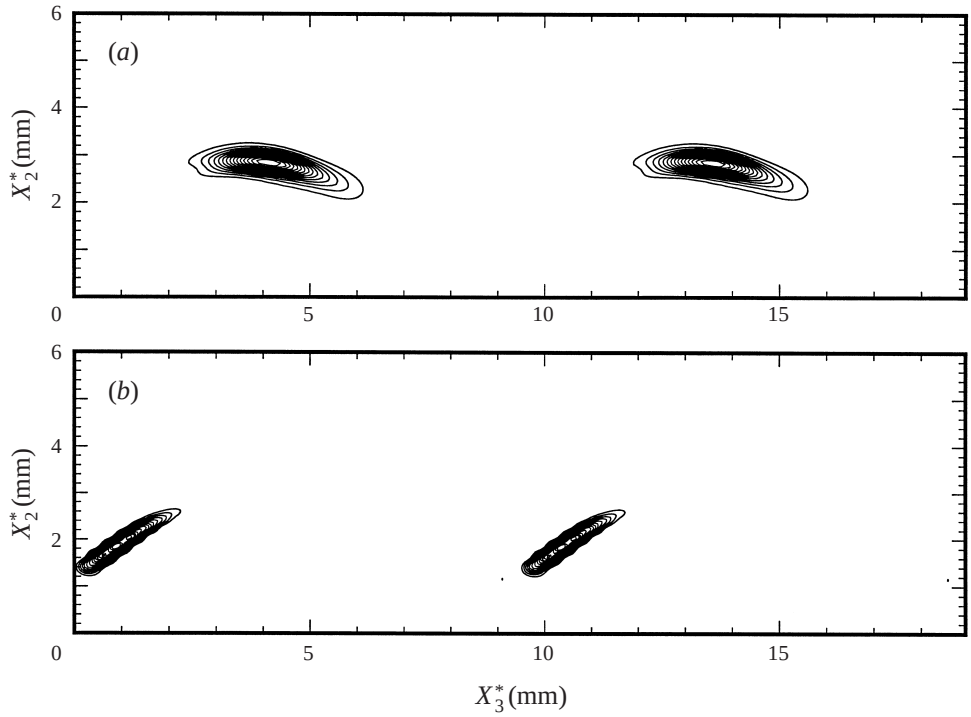

FIGURE 10. Contour plots of the production terms for Case I-A, $X^*/C = 0.4$. (*a*) $-\langle u_1 u_2 \rangle \partial U_1/\partial X_2$, $\alpha_s = 1.4\,\mathrm{mm}^{-1}$; (*b*) $-\langle u_1 u_3 \rangle \partial U_1/\partial X_3$, $\alpha_s = 1.2\,\mathrm{mm}^{-1}$.

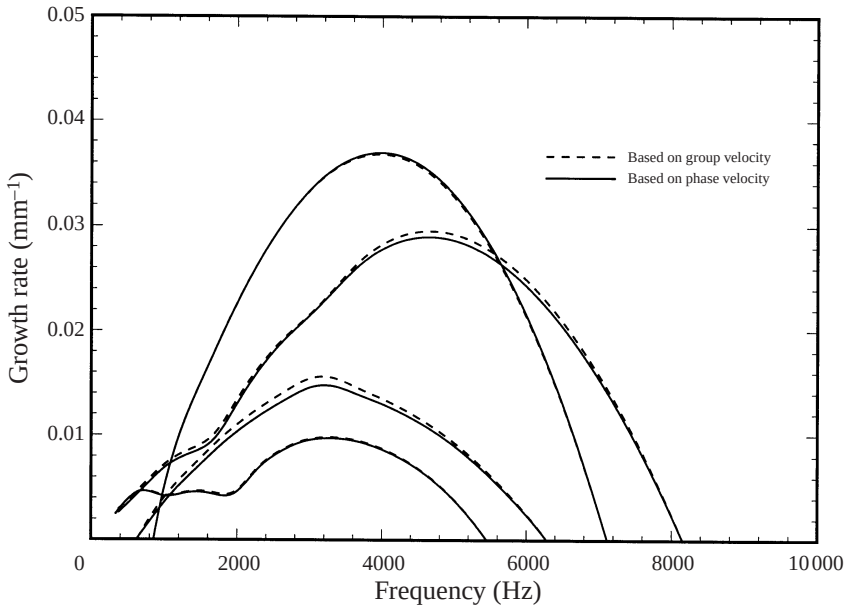

FIGURE 11. Comparison of spatial amplification rates based on group velocity and phase velocity, respectively, of secondary instability modes (Case I-C, $X^*/C = 0.35$).

for the secondary instability modes. Conversion of temporal amplification rates to spatial ones was accomplished using the approximation suggested by Gaster (1962). This transformation, which is based on a Taylor series expansion of the dispersion relation about the real frequency axis, uses the group velocity of the disturbance to convert the disturbance growth in time to growth in space. However, because the secondary instability modes are nearly non-dispersive and the phase velocity of these modes is nearly the same as their group velocity, the phase velocity was used instead during the above transformation. The accuracy of this approximation can be gleaned from the sample comparison plotted in figure 11.

Typically, N-factor correlation for a given flow is obtained by integrating either the maximum local growth rate of any instability mode (the 'envelope' method) or by maximizing over the local amplification ratio (i.e. integrated growth rate) of a fixed disturbance entity. The latter method, which makes more physical sense, was used earlier to obtain the N-factor curves for primary instability modes. However, it cannot be easily implemented within the context of secondary instability modes, because of the relatively sparse streamwise locations at which the secondary instability analysis was carried out. Because of the difficulties involved in establishing topological connections between the various modes at any pair of adjacent chordwise locations, the N-factor curves were computed by lumping together all the modes of a given type (i.e. all 'y' or all 'z' modes). Thus, the local growth rate of the secondary instability at a given physical frequency was determined through maximization over all the unstable modes of a specified type. As with the N-factor correlation based on primary instability, the maximum value of the N-factor at the experimentally determined transition location was used for the purposes of correlation.

Implicit in the above procedure is the assumption that the most unstable mode of a given type represents the same disturbance entity at all chordwise locations. An examination of the relevant eigenfunctions and the overall growth rate behaviour suggests that the above assumption is a reasonable one. However, it is difficult to guarantee its validity in view of the multiple number of unstable modes present in the problem (as well as the occasional mode crossing involved). We also wish to note that, for a given set of test conditions, the shift in the peak growth rate frequency with respect to chordwise location is relatively small. Hence, the N-factor correlation obtained with the above technique is also expected to be close to that based on the envelope method (wherein the growth rate is maximized locally with respect to all unstable modes and all relevant frequencies).

Secondary 'z' mode N-factor results for Cases I-A–I-C are given in figure 12(a–c). Within the region of secondary instability, the peak linear growth rates of the secondary instability modes tend to be significantly larger than those of the primary modes. For instance, in Case I-A, the N-factor for the secondary modes increases by nearly 8 between the range of locations $X^*/C \in [0.35, 0.50]$. The corresponding increase in the N-factor for the (linear) primary instability is approximately 2. Of course, because of the nonlinear effects, the actual increase in the amplitude ratio for the primary modes is even smaller. The above comparison confirms the rapid onset of the secondary instability and, hence, lends credence to the use of the quasi-parallel assumption for the nonlinearly distorted boundary-layer flow.

The N-factor correlations obtained by combining the secondary instability results with the experimental data of table 1 are summarized in table 3. Also included in table 3 are the computed values of the primary disturbance amplitude at measured transition locations (except for Case II-E) and the associated N-factor (nonlinear) based on the integral of the disturbance kinetic energy. The primary disturbance

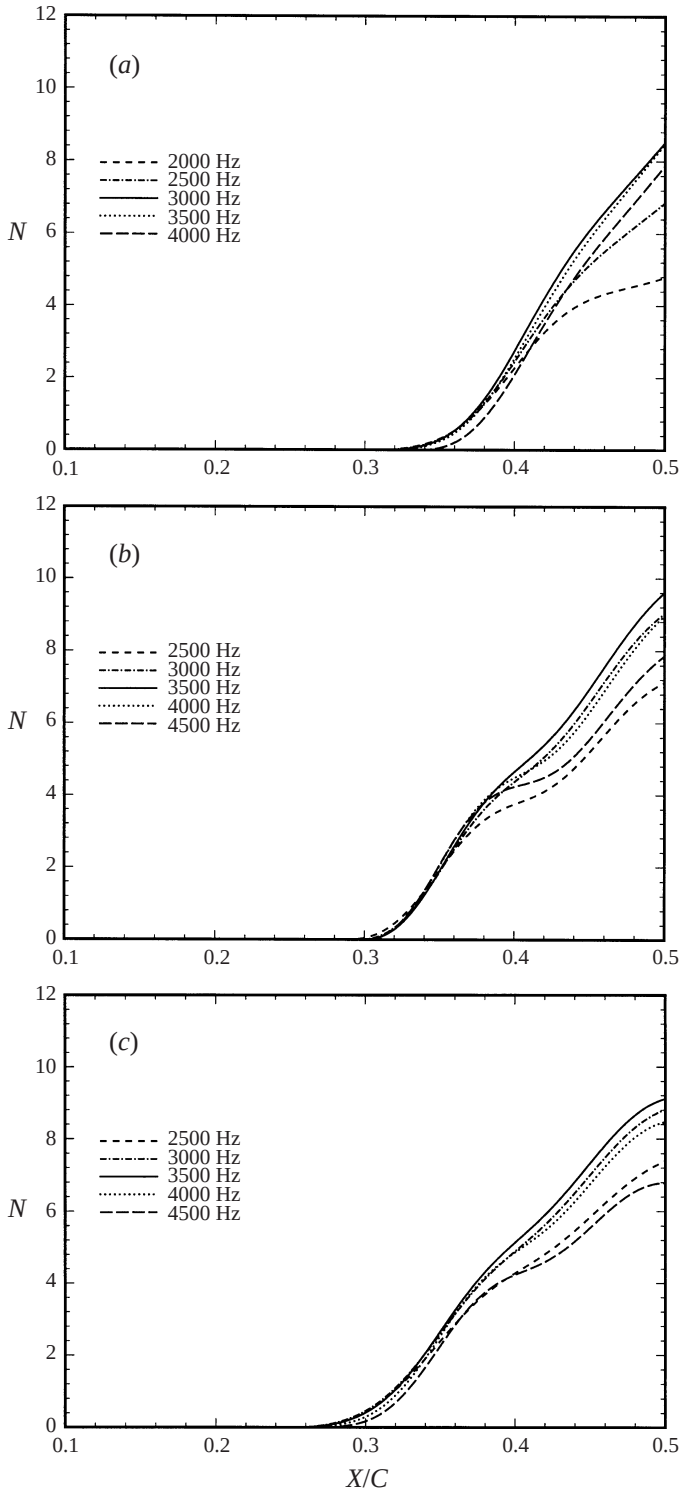

FIGURE 12. *N*-factor curves for the '*z*'-type secondary instability modes. (*a*) Case I-A; (*b*) Case I-B; (*c*) Case I-C.

Case	Transition location $(X^*/C)_{tr}$	Secondary modes N_y	Freq.$_y$ (kHz)	N_z	Freq.$_z$ (kHz)	Primary modes Amplitude (total r.m.s.)	Amplitude (modal)	$N_{primary}$
I-A	0.52	11.2	4.5	9.4	3.0	0.188	0.175	5.82
I-B	0.51	11.0	4.5	10.0	3.5	0.185	0.180	5.01
I-C	0.49	10.9	4.5	8.9	3.5	0.179	0.173	4.24
I-D	0.32	4.2	7.0	—	—	0.166	0.151	5.66
I-E	0.30	6.5	8.5	—	—	0.171	0.148	4.56
II-E	0.70	—	—	3.3†	2.5	0.102†	0.101†	—

† Value at $X^*/C \approx 0.35$.

TABLE 3. N-factor results at $(X^*/C)_{tr}$ for secondary instability modes and the amplitudes of the primary modes.

amplitudes quoted herein reflect the computed approximations to experimentally determined amplitudes. Based on the streamline orientations in the mid-chord region, we expect the above approximations for amplitude to be nearly the same as that based on the peak velocity perturbation (normalized by the local edge velocity) along the direction of the inviscid streamline.

It should be noted here that, while transition occurred at $X^*/C = 0.7$ for Case II-E, secondary instability calculations were performed only up to $X^*/C \approx 0.35$ where the secondary N-factor reached a value of 3.3. This value of the N-factor is considerably smaller than the N-factor values that correlate with the transition onset location in the other cases, confirming the experimental finding that transition is delayed in the presence of artificial roughness with wavelength smaller than the dominant wavelength. Computation of secondary instability in the region downstream of $X^*/C > 0.35$ will require a new basic-state calculation that includes the naturally occurring crossflow disturbances as noted in § 4.3. Nonlinear PSE calculations of this type were performed which showed the suppression of longer wavelength stationary modes by the shorter wavelength forced mode. However, the secondary instability calculation for the broadband basic state requires substantially larger computer memory and CPU time and, therefore, was not attempted during the present study.

Let us now examine the N-factor results for Cases I-A–I-E. First observe that the variation in secondary instability N-factor with respect to roughness height is small when all the data points at a fixed Reynolds number are considered, except that the values of N-factors for the $Re = 3.2 \times 10^6$, cases (namely I-D and I-E) are smaller than those at $Re = 2.4 \times 10^6$. Fortunately, this discrepancy does not have serious consequences. Because of the rapid growth of secondary instability modes, especially at $Re = 3.2 \times 10^6$, using a larger value for the N-factor will simply lead to a small downstream shift in the predicted transition location. We obtain the optimal value of N-factor for the set of Cases I-A–I-E by minimizing the root-mean-square (r.m.s.) error in the predicted transition location, where r.m.s. error is defined as

$$\left\{ \sum_{\text{overall cases}} \frac{(x_{tr\text{-measured}} - x_{tr\text{-predicted}})^2}{n} \right\}^{1/2},$$

where n is the number of cases. To help determine this optimum value, in table 4 we present the predicted transition locations for various assumed values for the N-factor.

			Secondary N-factor								
Case	$(X^*/C)_{tr}$	Type	10.0	9.5	9.0	8.5	8.0	7.5	7.0	6.5	6.0
I-A	0.52	y	0.497	0.488	0.479	0.469	0.460	0.450	0.441	0.431	0.422
I-B	0.51	y	0.490	0.480	0.469	0.457	0.445	0.431	0.419	0.407	0.396
I-C	0.49	y	0.465	0.451	0.435	0.420	0.405	0.390	0.381	0.367	0.356
I-A	0.52	z	—	—	—	0.500	0.489	0.481	0.471	0.462	0.452
I-B	0.51	z	—	0.497	0.486	0.476	0.468	0.459	0.451	0.443	0.433
I-C	0.49	z	—	—	0.493	0.476	0.464	0.453	0.444	0.433	0.422
I-D	0.32	y	0.388	0.382	0.376	0.370	0.364	0.358	0.352	0.347	0.340
I-E	0.30	y	0.355	0.347	0.339	0.322	0.330	0.315	0.307	0.300	0.292

TABLE 4. Transition correlation based on N-factor for secondary instability modes.

		Total r.m.s. primary amplitude								
Case	$(X^*/C)_{tr}$	0.12	0.13	0.14	0.15	0.16	0.17	0.18	0.19	0.20
I-A	0.52	0.310	0.332	0.356	0.382	0.408	0.435	0.464	0.497	—
I-B	0.51	0.247	0.262	0.296	0.359	0.378	0.395	0.425	—	—
I-C	0.49	0.212	0.225	0.243	0.340	0.362	0.380	0.404	—	—
I-D	0.32	0.223	0.232	0.241	0.250	0.268	—	—	—	—
I-E	0.30	0.163	0.172	0.179	0.183	0.195	0.208	0.392	0.408	0.425

TABLE 5. Transition correlation based on total primary amplitude.

		Modal primary amplitude								
Case	$(X^*/C)_{tr}$	0.12	0.13	0.14	0.15	0.16	0.17	0.18	0.19	0.20
I-A	0.52	0.315	0.342	0.373	0.403	0.430	0.465	0.489	—	—
I-B	0.51	0.249	0.270	0.352	0.375	0.392	0.420	—	—	—
I-C	0.49	0.215	0.230	0.339	0.360	0.380	0.400	—	—	—
I-D	0.32	0.225	0.233	0.244	0.258	—	—	—	—	—
I-E	0.30	0.164	0.175	0.180	0.190	0.205	0.412	0.428	0.450	—

TABLE 6. Transition correlation based on modal primary amplitude.

Analogous data for the transition criterion based on the total and modal amplitudes of the primary disturbance are presented in tables 5 and 6, respectively. Variation of the root-mean-square error in the predicted transition location as a function of the N-factor and the total or modal disturbance amplitude is plotted in figures 13(a) and 13(b), respectively.

A comparison between figures 13(a) and 13(b) shows that the expected error in transition prediction based on secondary instability growth rates is significantly smaller than that based on the primary disturbance amplitude. Indeed, the optimal N-factor of 8.5 in the former case compares favourably with the experimental findings of Kohama *et al.* (1996), who measured an N-factor of slightly more than 9 for the secondary instability modes prior to transition. In addition, the secondary N-factor criterion is seen to be more robust to variations in the basis of the correlation (i.e. the optimal N-factor in figure 13a). For instance, within a band of N-factors ranging from 8.5 to 6.0, the error in the predicted transition location remains within a narrow band of approximately 3 to 4% of the airfoil chord (i.e. about 10% of the mean transition location of $X^*/C = 0.43$). This is because the sensitivity is inversely

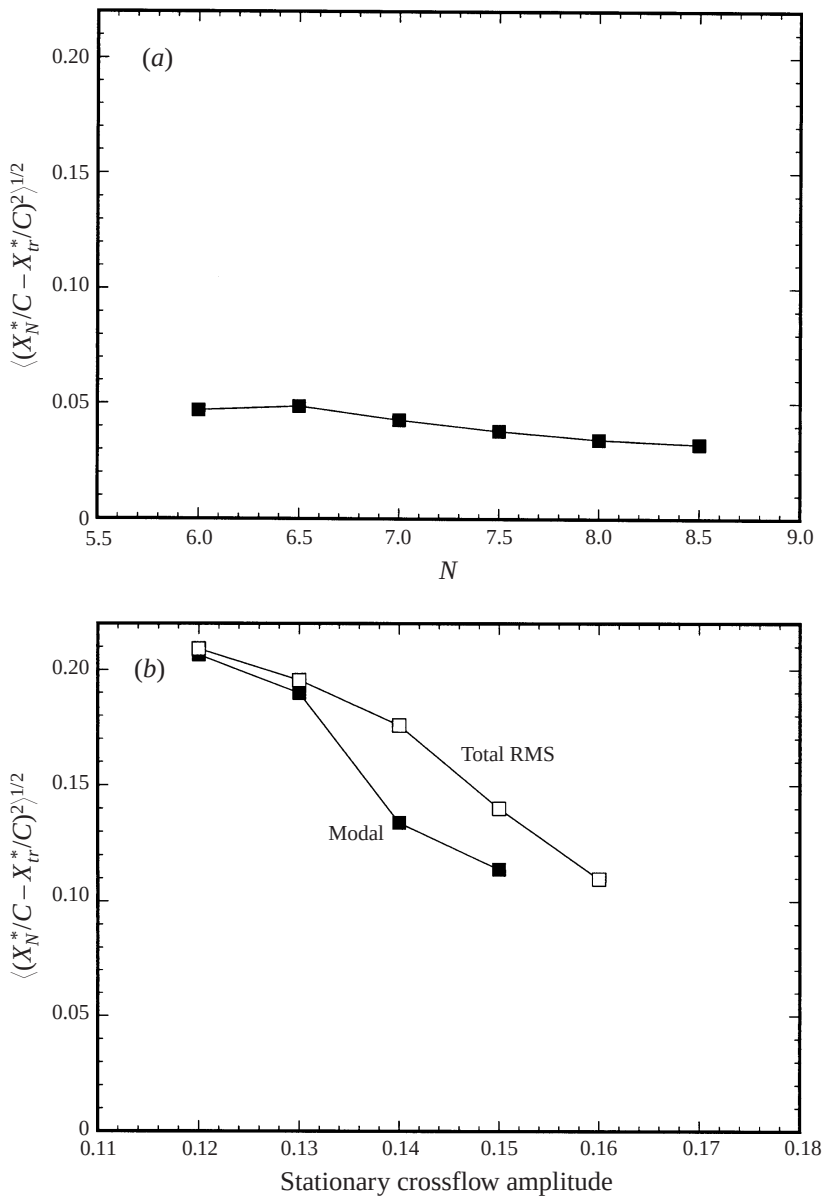

FIGURE 13. Expected error in transition prediction based on N-factor correlation for secondary instability modes and primary disturbance amplitude. (*a*) secondary N-factors; (*b*) disturbance amplitude.

proportional to the slope of the N-factor curve. It can be seen from figure 12(*a–c*) that the value of the N-factor varies relatively rapidly with X^*/C and, therefore, the predicted transition location varies little when the transition N-factor is changed within a reasonable range. On the other hand, owing to its slow variation, the error in transition prediction based on the primary disturbance amplitude increases relatively rapidly as the assumed amplitude is reduced. This finding is consistent with our earlier forecast that was based on the slow (and possibly non-monotonic) variation in primary disturbance amplitude across a significant region upstream of transition

location. Note that the error levels for the transition criteria based on both measures of the primary amplitude (i.e. total and modal) are nearly the same, because, in all of the five cases studied herein, the total primary disturbance amplitude is dominated by its fundamental harmonic.

5. Discussion

Results from experimental measurements of disturbance evolution in a controlled setting have been used to validate the advanced transition prediction tools and to examine their potential for providing enhanced physical understanding and refined predictive capability. Similar to the earlier findings by Radeztsky *et al.* (1993) in the ASU facility, the measurements by Reibert *et al.* (1996) and Carrillo *et al.* (1996) demonstrate the importance of including information about the initial disturbance spectrum (i.e. the outcome of the receptivity phase) in the transition prediction process. Even more significantly, their data show the inadequacies of an approach that is based on just the receptivity and linear amplification phases, i.e. an approach that ignores the nonlinear development of the primary instability modes. Two methods that meet the above requirements and, hence, have the potential to successfully explain the findings of Reibert *et al.* and Carrillo *et al.* were investigated in the present work. These methods correlated the measured transition location with the nonlinearly computed primary disturbance amplitude and with the N-factor based on linear growth of secondary instability modes, respectively. The latter approach requires additional effort as well as significantly higher computational resources in terms of both memory and CPU time. However, at least within the limited context of the experimental data points examined herein, the secondary N-factor approach delivers more accurate and more robust transition onset predictions. Following additional code development and continued increase in computer memory and speed, the above technique would become more practical, at least as a means to obtain additional insights during the final stages of the aerodynamic design process.

To further improve the reliability of the above technique, it is necessary to repeat similar calculations for a larger set of experiments, preferably from more than a single facility. The data sets by Radeztsky *et al.* (1993) in the same ASU facility (which included a broader variation in the Reynolds number and the initial crossflow amplitude), and the recent experiments by Kohama *et al.* (1996) (in which the structure of the secondary instability was examined in further detail), as well as Deyhle & Bippes (1996), are particularly promising in this regard. Also important from the standpoint of practical applications are additional calculations involving relatively broadband stationary crossflow disturbances. Analysis of these problems will require larger computational resources, and/or the development of more sophisticated computational procedures, or even additional simplifying assumptions that may be specific to the case of interest.

During previous work in the ASU facility, Radeztsky *et al.* (1993) conducted a comprehensive study of the effect of initial crossflow disturbance amplitudes on the location of transition onset. Their results indicate that, for initial amplitudes that are greater than some critical value but still relatively small, the transition location moves progressively further upstream as the initial crossflow amplitude is increased. However, the rate of upstream movement slows down at larger initial amplitudes, almost asymptoting to a fixed transition location. Cases I-A–I-E examined herein fall under the latter regime wherein the location of transition onset is nearly independent of the roughness height. The present calculations must be extended to smaller initial

amplitudes to confirm their ability to predict the downstream shift, in particular towards the transition location measured in the absence of any artificial roughness. The accompanying improvement in the accuracy of an amplitude criterion based on the linear N-factors also needs to be quantified.

A possible shortcoming of the advanced transition prediction approaches examined herein is the additional input required concerning the initial disturbance amplitudes. These amplitudes vary linearly with the roughness height in the limit of small roughness amplitudes. However, the initial amplitudes required to match the nonlinear PSE results with the measured data were found to increase at a slower than linear rate when the roughness height was increased from 6 μm (Case I-A) to 48 μm (Case I-C).

Finally, additional experiments (see, however, the recent experiments of Kawakami *et al.* 1999) that investigate the spatial structure of the secondary instability modes and provide details of disturbance evolution across the transition region are necessary to establish a firmer link between transition onset and secondary instability. Experiments of this kind will also provide clues to the origin of the secondary instability as well as helping us to identify the factors (besides the growth rates) that determine what type of secondary instability mode will be observed in practice. Work needs to be done on the receptivity of the boundary layer to the imposed disturbance field. This would eliminate the need for the somewhat *ad hoc* matching of the initial amplitudes used in the present study. The possibility of absolute instability of the secondary modes remains to be investigated. Also required are spatial simulations that include both stationary and non-stationary crossflow modes, as well as including the effect of nonlinear interactions on the evolution of secondary instability. Resources required for investigations of this type are relatively substantial, but so is the potential payback in terms of increased physical understanding, and better methods for prediction and control of transition in three-dimensional boundary layers. The work of Högberg & Henningson (1998), which appeared after the first submission of this manuscript, is a step in that direction. The direct Navier–Stokes simulations performed by these authors were able to capture stationary/travelling crossflow mode interaction as well as the high-frequency secondary instability predicted by Malik *et al.* (1994). Based on their simulation results, they concluded that '... the streamwise location of the start of transition should be well correlated with the neutral point of the high-frequency instability, since the turn-on of the instability is quite rapid and high values of the growth rate are reached quickly'. While the present results, and those of Malik *et al.* (1994), indicate that the secondary instability grows relatively fast, the correlation of transition onset location with the onset of secondary instability is not generally supported by the present results. The r.m.s. error for the cases in figure 12 will be substantial if the neutral location for secondary instability is used for the correlation of transition onset.

6. Conclusions

We have used the parabolized stability equations (PSE) approach to investigate the nonlinear development of stationary crossflow disturbances in an infinite-swept-wing boundary layer. More specifically, the conditions of the experiments of Reibert *et al.* (1996) and Carillo *et al.* (1996) are investigated. The nonlinearly distorted mean flow is analysed for secondary disturbances using a two-dimensional eigenvalue approach. The following conclusions can be drawn from this study:

1. Computed results (present and those of Haynes & Reed 1996) for the evolution of disturbance amplitudes are in good agreement with the experimental observations.

2. The distorted mean flow is subject to secondary instability and a number of modes (up to 7) have been found. These modes belong to two basic families: one associated with wall-normal shear and the other with the spanwise shear. In that sense, these modes are akin to the 'horseshoe' and 'sinuous' modes of the Görtler vortex problem.

3. Owing to the slow variation of crossflow disturbance amplitudes in the nonlinear regime, an absolute amplitude based criterion does not yield a good correlation of the transition onset location. In contrast, an N-factor approach based on the secondary disturbance growth rates yields a much more robust correlation. The value of the optimal secondary N-factor (~ 8.5) is quite close to the experimental value found by Kohama *et al.* (1996).

4. The present approach confirms the experimental finding that transition onset can be delayed by suitably placed roughness with a spanwise wavelength that is shorter than the wavelength of the most amplified (natural) disturbance in the boundary layer.

This work was carried out under a sub-contract from Boeing ZA0095 (NASA Contract NASI-20267) with Dr Paul Johnson as the Technical Monitor. The authors would like to thank Professor W. S. Saric, Dr Mark Reibert, and Mr Ruben Carrillo, Jr for providing the data acquired in the ASU experiment. Thanks are also due to Drs Ronald Radeztsky and Ray-Sing Lin, both of HTC, for their assistance with interpretation of experimental data and global eigenvalue calculations, respectively.

REFERENCES

Bertolotti, F. P., Herbert, Th. & Spalart, P. R. 1992 Linear and nonlinear stability of the Blasius boundary layer. *J. Fluid Mech.* **242**, 441–474.

Carrillo, R. B., Jr., Reibert, M. S. & Saric, W. S. 1996 Distributed roughness effects on stability and transition in swept-wing boundary layers. Final Report for NASA LaRC Cooperative Agreement NCC-1-194.

Chang, C.-L. & Malik, M. R. 1994 Oblique-mode breakdown and secondary instability in supersonic boundary layers. *J. Fluid Mech.* **273**, 323–359.

Chang, C.-L., Malik, M. R., Erlebacher, G. & Hussaini, M. Y. 1991 Compressible stability of growing boundary layers using parabolized stability equations. *AIAA Paper* 91-1636.

Crouch, J. D. 1997 Transition prediction and control for airplane applications. *AIAA Paper* 97-1907.

Deyhle, H. & Bippes, H. 1996 Disturbance growth in an unstable three-dimensional boundary layer and its dependence on environmental conditions. *J. Fluid Mech.* **316**, 73–113.

Gaster, M. 1962 A note on the relationship between temporarily increasing and spatially increasing disturbances in hydrodynamic instability. *J. Fluid Mech.* **14**, 222–224.

Gaster, M. 1967 On the flow along swept leading edges. *Aeron. Q.* **XVIII**, 165–184.

Gregory, N., Stuart, J. T. & Walker, W. S. 1955 On the stability of three-dimensional boundary layers with application to the flow due to a rotating disk. *Phil. Trans. R. Soc. Lond.* A **248**, 155–199.

Hall P. & Horseman, N. J. 1991 The linear inviscid secondary instability of longitudinal vortex structures in boundary layers. *J. Fluid Mech.* **232**, 357–375.

Haynes, T. 1996 Nonlinear stability and saturation of crossflow vortices in swept-wing boundary layers. PhD dissertation, Arizona State University, Tempe, AZ.

Haynes, T. & Reed, H. L. 1996 Computations in nonlinear saturation of stationary crossflow vortices in a swept-wing boundary layer. *AIAA Paper* 96-0182.

Herbert, Th. 1991 Boundary-layer transition–analysis and prediction revisited. *AIAA Paper* 91-0737.

Högberg, M. & Henningson, D. 1998 Secondary instability of cross-flow vortices in Falkner–Skan–Cooke boundary layers. *J. Fluid Mech.* **368**, 339–357.

Janke, E. & Balakumar, P. 1998 Nonlinear stability of three-dimensional boundary layers. *AIAA Paper* 98-0337.

Kawakami, M., Kohama, Y. & Okutsu M. 1999 Stability characteristics of stationary crossflow vortices in three-dimensional boundary layer. *AIAA Paper* 99-0811.

Koch, W. 1992 On a degeneracy of temporal secondary instability modes in Blasius boundary-layer flow. *J. Fluid Mech.* **23**, 319–351.

Kohama, Y., Onodera, T. & Egami, Y. 1996 Design and control of crossflow instability field. In *Proc. IUTAM Symp. on Nonlinear Instability and Transition in Three-Dimensional Boundary Layers, Manchester, UK* (ed. P. W. Duck & P. Hall), pp. 147–156. Kluwer.

Kohama, Y., Saric, W. S. & Hoos, J. A. 1991 A high frequency, secondary instability of crossflow vortices that leads to transition. *Proc. R. Aeronaut. Soc. Conf. on Boundary-Layer Transition and Control, Cambridge*, UK, pp. 4.1–4.13.

Li, F. & Malik M. R. 1995 Fundamental and subharmonic secondary instability of Görtler vortices. *J. Fluid Mech.* **297**, 77–100.

Li, F. & Malik, M. R. 1996 On the nature of PSE approximation. *Theor. Comput. Fluid Dyn.* **8**, 253–273.

Li, F. & Malik, M. R. 1997 Spectral analysis of parabolized stability equations. *Computers Fluids* **26**, 279–297.

Lin, R.-S., Li, F. & Malik M. R. 1999 Response of swept leading-edge flows to line impulsive excitation. *AIAA Paper* 99-0815.

Lin, R.-S. & Malik, M. R. 1996 On the stability of attachment-line boundary layers. Part 1. The incompressible swept Hiemenz flow. *J. Fluid Mech.* **311**, 239–255.

Lin, R.-S., Wang, W.-P. & Malik, M. R. 1996 Linear stability of incompressible viscous flow along a corner. In *1996 Fluids Engng Div. Conf.* FED 237, vol. 2. ASME.

Lingwood, R. J. 1995 Absolute instability of the boundary layer on a rotating disk. *J. Fluid Mech.* **299**, 17–33.

Lingwood, R. J. 1997 On the impulse response for swept boundary-layer flows. *J. Fluid Mech.* **344**, 317–334.

Malik, M. R. 1997 Boundary-layer transition prediction toolkit. *AIAA Paper* 97-1904.

Malik, M. R. & Li, F. 1992 Three-dimensional boundary layer stability and transition. *SAE Paper* 921991.

Malik, M. R., Li, F. & Chang, C.-L. 1994 Crossflow disturbances in three-dimensional boundary layers: nonlinear development, wave interaction and secondary instability. *J. Fluid Mech.* **268**, 1–36.

Malik, M. R., Li, F. & Chang, C.-L. 1996 Nonlinear crossflow disturbances and secondary instabilities in swept-wing boundary layers. In *Proc. IUTAM Symp. on Nonlinear Instability and Transition in Three-Dimensional Boundary Layers, Manchester, UK* (ed. P. W. Duck & P. Hall), pp. 257–266. Kluwer.

Poll, D. I. A. 1979 Transition in the infinite swept attachment line boundary layer. *Aeronaut. Q.* **30**, 607.

Poll, D. I. A. 1985 Some observations of the transition process on the windward face of a long yawed cylinder. *J. Fluid Mech.* **150**, 329–356.

Radeztsky, R. H., Jr., Reibert, M. S., Saric, W. S. & Takagi, S. 1993 Effect of micron sized roughness on transition in swept-wing flows. *AIAA Paper* 93-0076.

Reibert, M. 1996 Nonlinear stability, saturation, and transition of crossflow-dominated boundary layers. PhD dissertation, Arizona State University, Tempe, AZ.

Reibert, M., Saric, W. S., Carrillo, R. B., Jr & Chapman, K. L. 1996 Experiments in nonlinear saturation of stationary crossflow vortices in a swept-wing boundary layer. *AIAA Paper* 96-0184.

Stevens, W. A., Goradia, S. H. & Braden, J. A. 1971 A mathematical model for multi-component airfoils in viscous flow. *NASA CR*-1843.

Swearingen, J. D. & Blackwelder, R. F. 1987 The growth and breakdown of streamwise vortices in the presence of a wall. *J. Fluid Mech.* **182**, 255–290.

Wie, Y.-S. 1992 BLSTA – A Boundary layer code for stability analysis. *NASA Contractor Rep.* 4481.

Yu, X. & Liu, J. T. C. 1991 The secondary instability in Görtler flow. *Phys. Fluids* A **4**, 1825–1827.

Yu, X. & Liu, J. T. C. 1994 On the mechanism of sinuous and varicose modes in three-dimensional viscous secondary instability of nonlinear Görtler rolls. *Phys. Fluids* **6**, 736–750.